OPEN ACCESS
IOP Publishing
Journal of Physics G: Nuclear and Particle Physics
J. Phys. G: Nucl. Part. Phys. **47** (2020) 045116 (48pp)
https://doi.org/10.1088/1361-6471/ab67e9

Nuclear spectrometry of 9.6 h $^{196}Au^{m2}$ and the reaction of ^{197}Au with fast neutrons

K J Moody, N Gharibyan[3], D A Shaughnessy, P M Grant, J M Gostic[1], C J Cerjan, C B Yeamans, J D Despotopulos and S A Faye[2]

Lawrence Livermore National Laboratory, 7000 East Ave., Livermore, CA 94550, United States of America

E-mail: gharibyan1@llnl.gov

Received 13 August 2019, revised 7 December 2019
Accepted for publication 6 January 2020
Published 9 March 2020

Abstract

The neutron activation of gold is the basis of an implosion performance diagnostic at the National Ignition Facility at Lawrence Livermore National Laboratory. In support of this diagnostic, a series of γ-ray spectrometric measurements of the decay of $^{196}Au^{m2}$ ($J^{\pi} = 12^{-}$) was performed to improve the currently accepted literature values of the nuclear data associated with its half-life, γ-ray energies, and γ-ray intensities. It was determined that $^{196}Au^{m2}$ decays with a half-life of 9.603 h $\pm$ 0.23%. The relative intensities of the γ rays emitted during its decay were also measured, and an absolute decay branch of 0.3352 $\pm$ 2.9% was determined for the emission of the 188.2 keV photon, which arises from a nuclear transition whose multipolarity is predominantly $M1$. Properties of other products arising in the reaction of ^{197}Au with fast neutrons were measured, as were selected production cross sections. The $^{196}Au^{m2}/^{196}Au^{g}$ isomer ratio measured in the $^{197}Au(n, 2n)$ reaction at 14.1 MeV was found to be 0.0731 $\pm$ 2.6%.

Keywords: nuclear spectrometry, half-life, isomer ratio, gold, fast neutrons

(Some figures may appear in colour only in the online journal)

[1] Present address: Patrick Air Force Base, Brevard County, Fl 32925, United States of America.
[2] Present address: New York State Department of Health, Albany, NY 12201, United States of America.
[3] Author to whom any correspondence should be addressed.

1. Introduction

Measurement of the concentrations of the reaction products of the neutron activation of gold provides a diagnostic of fusion capsule performance [1] at the National Ignition Facility (NIF) at Lawrence Livermore National Laboratory (LLNL) [2]. In a typical NIF fusion experiment, a small capsule made of plastic, high density carbon, or beryllium, and containing a mixture of ^{2}H and ^{3}H, is suspended at the geometric center of a thin-walled cylindrical tube (the hohlraum [3]), which is constructed of approximately 0.1 g of heavy metals, primarily gold [4] (figure 1). The capsule is nominally 2 mm in diameter and the hohlraum dimensions are approximately 0.6 cm in diameter by 1 cm long. The hohlraum (and any associated cryonics) is placed precisely at the center of the 10 m diameter NIF vacuum chamber. Approximately 1 MJ of ultraviolet light is delivered by 192 lasers through the ends of the hohlraum (the laser entrance holes) over the time span of nanoseconds. The laser beams irradiate the inner surface of the hohlraum wall, producing a bath of *x*-ray photons that ablate the outer surface of the capsule, creating a 'spherical rocket' that rapidly compresses the thermonuclear fuel to densities beyond that found in normal terrestrial materials [5, 6]. The compressed capsule produces a pulse of neutrons several hundred picoseconds long [7] with a principal energy of 14.1 MeV, arising primarily from the ^{3}H(d, n)^{4}He reaction [5, 8, 9]. Capsule yields evolving more than 10^{16} neutrons have been achieved.

The degree to which the fuel is compressed, and its associated areal density, affects the probability that a thermonuclear neutron will scatter off the residual hydrogen fuel isotopes before escaping the fusion reaction site [1, 9]. Increased fuel density subsequently increases the fraction of the emitted neutrons that are down-scattered to energies below 14 MeV [10, 11]. The measured ratio of neutrons downscattered into the 10–12 MeV range relative to the unscattered primary 14.1 MeV neutrons emitted by the capsule (the down-scattered ratio, or DSR [11]) is related to the areal density $\langle \rho r \rangle$ of the fuel at the time of neutron production. The neutron spectrum at energies above 0.2 MeV can be measured promptly with neutron time-of-flight detectors and magnetic recoil spectrometers [12–14]; however, these measurements are performed at a distance several meters from the reaction site and subtend a solid angle that is only a small fraction of 4π. Neutron activation diagnostic measurements have demonstrated that there can be considerable directional anisotropy in the flux of neutrons emitted by the fusion capsule [15].

The time involved between the onset of laser irradiation and the emission of neutrons is sufficiently short that the hohlraum matrix does not move significantly from its initial position before it encounters the neutron flux, even though its inner surface has been heated to temperatures in excess of 0.1 keV [8]. The low energy portion of the neutron spectrum is much more likely to produce (n, γ) reaction products in the hohlraum than is the more intense spectral region near 14 MeV [16]. As a result, the ratio of the relative rates of the ^{197}Au(n, γ)^{198}Au and ^{197}Au(n, $2n$)^{196}Au reactions is an indicator of fuel compression. The proximity of the gold to the source of neutrons is a critical factor in the use of the isotope ratio as a diagnostic of capsule performance, since the neutron flux from the capsule at distances on the order of a centimeter overwhelms the (n, γ) contribution from low energy room return neutrons [9] (see section 5.4). The radiochemical measurement of gold isotopes in recovered debris samples is not prompt, requiring days for the complete analysis, but is less sensitive to neutron anisotropy than are the prompt techniques for measuring the down-scattered neutron fraction [1].

The collection of debris in the NIF environment is challenging [17–19] and is being developed as an areal-density diagnostic and for other proposed nuclear experiments at NIF [1, 20]. Following prompt irradiation with neutrons, the hohlraum matrix breaks apart and is

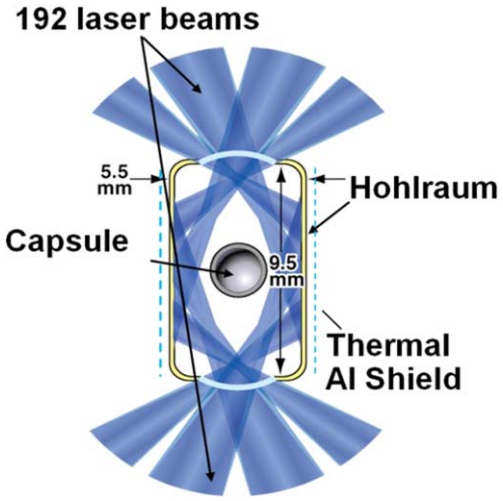

Figure 1. Illustration of the target assembly at the center of the NIF vacuum chamber including the 2 mm diameter capsule and the surrounding gold hohlraum.

propelled away from the center of the NIF chamber. The propulsive impulse arises from the deposited laser energy with very little contribution from the nuclear processes given the fusion yields achieved by NIF thus far [21]. The physical scale of the ejected debris, from atomic vapor to macroscopic particles, is an important issue for the integrity of fielded experiments and exposed laser optics components [22–24]. Debris samples for radiochemical analysis are collected passively at a distance 50 cm from the source of neutrons [25]. Foils of vanadium, tantalum or graphite, each with a diameter of 5 cm, are placed either near the plane defining the equator of the hohlraum or near the axis of the hohlraum. As many as 12 collectors can be deployed in an experiment. The mounting fixture leaves a 4 cm diameter exposed area on the surface of each collector (figure 2). The collection efficiency for hohlraum debris is impacted by the scale of the debris particles, the degree of melting on the collector surface, and the amount of ablation caused by the radiation front preceding the ballistic debris [1]. There is also considerable anisotropy in the distribution of debris to the individual collectors [25]. The collecting medium is activated by neutrons, which degrades the quantitative precision of the radionuclide measurements. In the case of particularly low-yield shots or stochastically poor collection efficiencies, radiochemical isolation and concentration of the desired products can be performed [26].

Radiochemical assays of the $^{196}Au^{m2}$ content of mixed radionuclide samples originating from inside the NIF chamber are routinely performed as part of the capsule performance diagnostic. The 9.6 h $^{196}Au^{m2}$ radionuclide is produced in the reaction of fast neutrons with the gold in the hohlraum. In performing these measurements, the intensities of the three strongest γ-rays emitted in the decay of $^{196}Au^{m2}$ in the samples are determined, and photon intensities reported in the literature [27] are used to calculate absolute decay rates. A weighted average over the three values is routinely reported as a diagnostic result. The uncertainty associated with the weighted average is given by the larger of the two values as calculated from the internal and external consistency methods (see section 4) [28]. For samples where the measured photon intensities have high statistical significance, it was observed that the standard deviation of the three measurements is much larger than the uncertainty on the propagated average, a strong indicator that the nuclear decay intensity data in the literature are

Figure 2. The Solid Radiochemistry (SRC) assembly [1] for collecting NIF debris at an equatorial position, in line with the waist of the hohlraum. As many as four 5 cm diameter collectors are mounted on a single support, which is placed in the center of the NIF chamber via the Diagnostic Instrument Manipulator (DIM). Once emplaced, the source of neutrons is 10 cm from the front of the conical nose cone part of the assembly and 50 cm from the SRC collector foils.

Table 1. Calculation of the $^{196}Au^{m2}$ content of representative debris sample CC6870 from NIF experiment N150416, first count after sample recovery, using literature [27] photon intensities for the three most intense γ lines. All errors are reported at one-sigma.

Photon energy (keV)	Measured photons/min	Spectroscopic relative intensity	Relative disintegrations/min
147.8	8199 ± 141	5.00	1639.8 ± 28.2
168.4	1100 ± 33	0.90 ± 0.05	1222.2 ± 77.2
188.3	6461 ± 85	3.45 ± 0.12	1872.8 ± 69.6
		Weighted average	1626 ± 111
		Normalization	0.087 ± 0.003
		Decay rate	18690 ± 1430

inadequate. As an example, table 1 shows the outline of the calculation of the absolute decay rate of $^{196}Au^{m2}$ at count time from a typical γ-ray spectrum taken from a solid debris collector after a NIF shot (see section 3). Details of the γ-spectroscopy are given in section 3 as well. The three determinations of the relative disintegration rate should have the same value, but instead vary substantially.

Though the decay intensities used in calculation of the $^{196}Au^{m2}$ activity may be inaccurate, the effect on the reported diagnostic ratio $^{198}Au/^{196}Au^{g}$ is minimal. The reported $^{196}Au^{m2}/^{196}Au^{m1+g}$ isotope ratio from the reaction of ^{197}Au with 14 MeV neutrons is approximately 0.07 [1, 29–31], and we determine $^{196}Au^{tot}$ based on γ counts taken more than two days following the irradiation after most of the 9.6 h $^{196}Au^{m2}$ (and short-lived $^{196}Au^{m1}$) has decayed to the 6.2 d ground state. Therefore, a substantial unquantified uncertainty that is part of a 7% correction to the $^{196}Au^{tot}$ content, which is used to extract the $^{196}Au^{g}$ content, has

no major impact on the propagated uncertainty attached to the resulting diagnostic ratio. Even so, the application of inadequate decay intensity information in the calculation of the $^{196}Au^{m2}$ content has created problems both in the interpretation of $^{196}Au^{m2}/^{196}Au^{g}$ as a potential diagnostic of capsule performance and for certain exotic physical processes [32, 33]. In the weaker signal debris collections produced at lower capsule yields fielded in the direction of the hohlraum laser entrance holes, the uncertainty in the determination of γ-ray intensities has a stronger contribution from the subtraction of the continuum than from the number of counts in the photopeak [34, 35]. This means that deficiencies in the decay intensity information can create a systematic bias in comparisons of the $^{196}Au^{m2}$ concentrations resulting from low- and high-yield fusion experiments, or in comparisons of collections of varying efficiency arising in the same experiment.

To improve the quality of the data associated with the analytical assays of NIF collection samples, a campaign to remeasure the nuclear data associated with the decay of $^{196}Au^{m2}$ was performed. The results from radiochemical experiments where pulses of high-energy neutrons arising from inertial confinement fusion capsules [36, 37] produced radionuclide sources that were used in the determination of the nuclear decay properties of $^{196}Au^{m2}$ are reported, as well as the measurement of cross sections for the reactions of ^{197}Au with thermonuclear neutrons.

2. Properties of the relevant gold isotopes

The ^{197}Au nucleus and those of nearby reaction products are spherical, lying beyond the region around $A = 190$ where nuclei near the line of β stability transition between the prolate shapes characterizing the rare earths and the spherical nuclei in the vicinity of doubly magic ^{208}Pb [38–40]. The experimental energy levels of odd–odd ^{196}Au have been interpreted with the nuclear shell model [41], but the problem is too complicated for the shell model to be predictive or incontrovertible [42]. The excited states in ^{196}Au are studied experimentally with particle stripping reactions [42, 43] and interpreted in the context of nearby nuclei with the interacting boson model [44], but the experiments are insensitive to high-spin states like those constituting $^{196}Au^{m2}$ ($J^{\pi} = 12^{-}$), which are far removed from the spin of the target nucleus.

The first report of isomeric states in the ^{196}Au nucleus was in 1937 [45], shortly after the discovery of artificially produced nuclear metastable species [46, 47]. Two activities produced in the reaction of fast neutrons with ^{197}Au were assigned to mass 196 based on a series of radiochemical measurements. A decade later [48, 49], a survey of the nuclear properties of isotopes of platinum and gold, produced in the bombardment of natural platinum with ^{2}H followed by the chemical isolation of gold, reported the same two activities with half-lives of approximately 5.55 d and 14 h. The properties of both radionuclides were studied, but the radiations emitted by the shorter-lived activity were less penetrating than those of the other gold activities and were difficult to quantify in detail.

In 1959 [50], weightless samples were prepared by the chemical isolation of gold following the ^{2}H irradiation of isotopically enriched ^{196}Pt. Conversion electron and scintillation spectrometry of characteristic emissions in the decay of the shorter-lived activity (half-life $= 10.0 \pm 0.5$ h) established that it underwent isomeric transition, and identified four γ transitions in cascade, one of which (175 keV) was a highly converted $M4$ transition that governs the decay rate. Several papers published in 1960 reported a half-life of approximately 10 h [51, 52], and that the $^{197}Au(n, 2n)$ reaction produced a more favorable isomer ratio than

did the ^{196}Pt(d, 2n), ^{197}Au(γ, n) [51], or high-energy ^{197}Au(p, pn) [53] reactions. An atomic beam experiment established that the ground state of ^{196}Au had a spin of 2 [54]; thus, the multipolarities of the internal transition photons in cascade required that the spin of the isomer be $\geqslant$ 11 [51, 52]. The ground-state decay was found to have a small branch for β^- decay, resulting in the emission of a 426 keV photon, with the rest of the γ-ray activity associated with the predominant EC decay [55–57]. A small branch for the EC decay of the metastable state was proposed [52], but could not be reproduced [41] (see section 5.6).

A measurement of the nuclear spin of the 10 h activity was performed with an atomic beam magnetic resonance apparatus [58], following the chemical isolation of gold from a sample of platinum irradiated with α particles [59]. The spin was found to be $J = 12$, and a negative parity was assigned based on a shell-model argument, which was later supported by experiment [60]. The structures of long-lived, high-spin, metastable states found subsequently in the odd–odd isotopes ^{198}Au [61, 62] and ^{200}Au [63, 64] are thought to be due to the same shell-model states, a $(\pi h_{11/2^-})(\nu i_{13/2^+})$ configuration [41, 65]. The angular momentum of ^{196}Au^{m2} is so high that reactions with neutrons and light charged particles do not produce a favorable isomer ratio until the reaction energy exceeds the peak for production of the isotope [66–69]. The (γ, n) reaction of ^{197}Au with Bremsstrahlung produces an even less favorable isomer ratio [70, 71]. These observations led to the use of heavy-ion reactions to produce a more favorable ^{196}Au^{m2}/^{196}Au^{g} isomer ratio [38, 72, 73], a technique which requires more study.

The half-lives of the ground and metastable states have been remeasured several times [56, 74–76]. Attempts to measure the isomer ratio more precisely in various reactions were hindered by a lack of quantitative nuclear intensity data for the photons emitted in the decay of the metastable state [77, 78]; these data were later improved in the mid-1960s [41, 76, 79]. At that time, delayed-coincidence techniques demonstrated that the lowest-energy transition (85 keV) in the four-member IT-decay cascade arose from a second metastable state [41, 80] with a half-life of less than 10 s. In a set of comprehensive experiments [41], sources prepared from ^{197}Au(n, 2n), $^{\text{nat}}$Pt(d, 2n), and ^{196}Pt(d, 2n) reactions were analyzed with photon and conversion-electron spectrometry employing coincidence techniques, resulting in the observation of several new γ transitions and a ^{196}Au level scheme similar to the one accepted today [27, 81] (figure 3).

The half-life of the ^{196}Au^{m1} isomeric state populated in the decay of ^{196}Au^{m2} was found to be 8.2 $\pm$ 0.2 s, decaying in a γ transition of $E3$ multipolarity [82]. The independent yield of ^{196}Au^{m1} in the ^{197}Au(n, 2n) reaction at 14 MeV was determined to be 0.2 relative to that of the ground state [82]; the cross section for production of the ground state given in the literature (and in this work) includes the cross section for the independent production of ^{196}Au^{m1}. The photon intensity of the highly converted 85 keV transition was often missed in early work, but data with reasonable statistics exist [82, 83].

One of the unresolved problems in the spectroscopy of ^{196}Au^{m2} is the placement of a 264 keV transition in the decay scheme [41]. It exhibits the same half-life as the rest of the ^{196}Au^{m2} transitions, so either connects states at or below the metastable state through internal transition, or is associated with other decay modes. The ground-state Q values for the other potential decay processes are $Q_{\beta^-} = 687 \pm 3$ keV and $Q_{\text{EC}} = 1506 \pm 3$ keV [84, 85]. Even though the ^{196}Au^{m2} state is almost 600 keV above the ground state, it is unlikely that high-spin states in the even–even daughter nuclei are at a sufficiently low excitation energy that their subsequent decays involving the emission of a 264 keV photon would not result in the emission of one or more additional photons of sufficient intensity to observe in our experiments (see section 5.6).

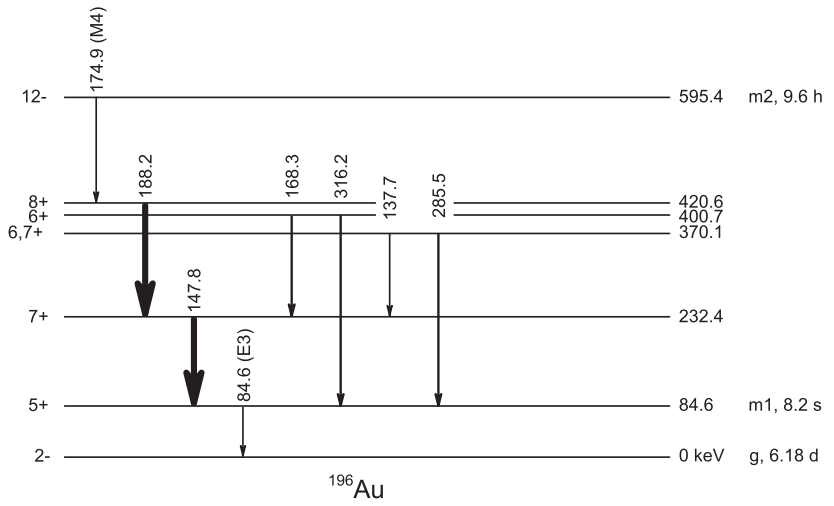

Figure 3. The ^{196}Au level scheme arising from the decay of $^{196}Au^{m2}$ [81] with transitions having energies above the *K* edge indicated. The weights of the arrows are a qualitative indication of intensity. There are several low-energy electromagnetic transitions between the states clustered near 400 keV, but they were not observed in the experiments described here.

The decay intensity data that we use in our radiochemical assay for $^{196}Au^{m2}$ in NIF experiments [1] are found in [27], an evaluation and review of the available literature data up to January 2006. In the evaluation, the best available experimental information [41] was found to be unconvincing, and the photon decay intensities were recalculated based on decay balances and theoretical models of internal conversion. Though the shortcomings of the literature decay intensity data were readily observed in collected NIF debris samples, it was decided not to use them as the basis of spectrometry experiments. Lateral inhomogeneity of the debris collections across the extended source areas introduces substantial undefined uncertainties in the detector/sample geometry. The presence of complicating contaminants from the activation of the hohlraum assembly also makes debris samples undesirable as sources for nuclear spectrometric measurements. A disadvantage to the ^{197}Au(n, $2n$) reaction for studying the properties of $^{196}Au^{m2}$ is the self-attenuation of low-energy γ-rays by the sample matrix [86]. As a result, gold target foils that were as thin as practical were used, consistent with the requirements of source intensity, to minimize the attenuation correction and the associated uncertainty. In preliminary experiments, the NIF neutron flux was limited and irradiations were performed with 5 cm diameter, 0.1 mm thick gold-foil targets that were mounted behind the NIF debris collectors. These data were discarded when NIF capsule yields improved, in part because of questions regarding the extended-source geometric correction applied by our γ analysis code and its interplay with the correction for self-attenuation by the relatively thick gold foils (see section 3.2).

Counting samples were produced by irradiating gold foils with fast neutrons at NIF as described in section 3. For experiments in which the radionuclides of interest are linked by decay, the 'instantaneous' character of a NIF irradiation has advantages over irradiations of extended duration performed at accelerator facilities. Immediately after the exposure of a target to the NIF neutron flux, the $^{196}Au^{m2}/^{196}Au^{m1+g}$ isotope ratio is equal to the ratio of the production cross sections, approximately 0.07. In an extended irradiation, saturation losses

Figure 4. (a) The Target Option Activation Device (TOAD) [88] shown as its separate components, which consist of the base plate with depression, the target foil stack that rests in the depression, and the cover plate, which is then epoxied over the target foil stack creating a single unit (shown in (b)) that can be fielded behind the SRC debris collectors seen in figure 2.

affect the inventory of the shorter-lived metastable nuclide [87], which decays to the ground-state nuclide during the time the source is being produced. These effects lead to a less favorable isotope ratio. As a means of studying ^{196}Au^{m2}, the ^{197}Au(n, $2n$) reaction as implemented at NIF is competitive with heavy-ion irradiations that have much more favorable cross-section ratios [38]. Details of the spectroscopy experiments conducted using NIF samples are described in section 3.

3. Experimental procedure

3.1. Irradiations and sample preparation

Experiments were performed using an apparatus for debris collections for diagnostic measurements that allowed for extra foil targets to be fielded during NIF shots. Targets for the production of spectrometry sources were introduced behind the DIM-mounted debris collectors (figure 2) at a fixed nominal distance of 50 cm from the neutron source. In the fixtures shown, compression springs hold the debris collectors in place against the retaining clamp. These springs are sufficiently compressible that samples with thicknesses of up to several mm can be accommodated behind the debris collectors.

The assembly shown in figure 2 that holds the collection foils is removed from the NIF chamber through a vacuum feedthrough shortly after the lasers fire. The cylindrical clamp on each fixture is removed to release the collector disks, which are transported to the radiochemistry facility where they are sealed in plastic for purposes of contamination control and then mounted for radiation counting. While chemical isolation of the hohlraum products from the surfaces of the collectors is possible, this procedure is generally not performed. The elapsed time between the lasers firing and the start of γ-ray counting is typically 3–6 h, but with prior preparation can be reduced to as little as 90 min.

The targets consisted of thin gold foils, nominally 2.5 cm in diameter, backed with thin aluminum foils to act as flux monitors via the ^{27}Al(n, α)^{24}Na reaction and to collect reaction products recoiling from the gold. The foils were fielded in sealed aluminum irradiation fixtures (Target Option Activation Device (TOAD); see figure 4), often as part of a stack of foils comprising other activation experiments [88]. The TOADs are 2 mm thick and 5 cm diameter, and can accommodate circular foils up to 2.5 cm diameter in a stack that can be as

Table 2. Experimental samples produced in five NIF irradiations. The experiment name incorporates the date on which the experiment was fielded, usually the day prior to irradiation on the given Julian date (in Pacific Daylight Savings Time). The empirical neutron yields are weighted values arising from several diagnostic measurements as supplied by the NIF diagnostics teams. The sample designators connect the experiment with the counting information provided in table 3.

Experiment ID	Year and Julian day	Neutron yield	Sample designator(s)
N130530	2013, day 151.147	$5.76(12) \times 10^{14}$	T13
N141106	2014, day 310.967	$2.77(6) \times 10^{15}$	T65
N141116	2014, day 321.146	$1.28(4) \times 10^{15}$	T61
N150416	2015, day 106.965	$7.03(12) \times 10^{15}$	T98
N151020	2015, day 294.627	$3.46(6) \times 10^{15}$	T62, T63, T64

thick as 0.6 mm. Targets of different materials are isolated from one another by thin aluminum foils; recoil losses of 15 h ^{24}Na from a backing foil are replaced by recoil from the upstream foil stack or the TOAD cover plate, validating the use of ^{27}Al as a flux monitor. The TOAD is sealed with an adhesive (figure 4(b)) that, after curing, can be reopened with mechanical force to release the irradiated foils.

Table 2 lists five NIF experiments in which seven gold samples were fielded for the spectrometric measurements of ^{196}Au^{m2} reported in this paper. The experiments spanned a 2.5-y period during which the performance of NIF improved markedly, as reflected in the increased neutron yields. The solid angle subtended by the target foils is approximately 1.5×10^{-4} of 4π, so table 2 can be used to estimate the neutron exposure of each sample.

Gold and aluminum samples recovered from the TOAD irradiation fixtures were positioned on aluminum counting disks and covered with layers of plastic foil and transparent plastic tape for a total thickness of 7 mg cm^{-2}. Only ^{24}Na and the radionuclides arising in the reactions of neutrons with gold were detected in counts of the samples. It was assumed that the radionuclide concentration of each activated source was uniform throughout the gold medium. While this was not true for ^{24}Na produced in the separate aluminum foils, the difference between the calculation of attenuation by the gold and self-attenuation for distribution through the gold was negligible for the high-energy photons emitted by ^{24}Na [89].

3.2. γ-ray spectrometry and spectral analysis

γ- and x-ray photons were measured with single semiconductor germanium photon detectors [90]. A representative spectrum (sample T63) is shown in figure 5. The counting electronics and acquisition hardware were standard for the collection of spectral data as singles [90]. The detectors were calibrated for both energy and efficiency responses with a set of standards [91], including commercial NIST-traceable mixed-radionuclide sources, and locally produced sources of ^{152}Eu, ^{241}Am, and ^{182}Ta [92–94]. The energy dependence of the efficiency function arises from a geometric model based on the construction of the detectors, benchmarked against the calibration standards. From figure 3 we know that coincident summing of photons emitted sequentially in the decay of ^{196}Au^{m2} is a potential problem. The most intense γ-rays emitted in the EC decay of ^{196}Au are also partially sequential [27]. A source of ^{166}Ho^{m} [95, 96] was used to check the effects of sample/detector distance on coincident summing of sequentially emitted photons having energies comparable to those emitted in the decay of ^{196}Au^{m2}; this information was used to characterize a minimum detector/source distance in each experiment. Photons emitted in the decays of ^{196}Au^{g} and ^{198}Au^{g} in the experimental

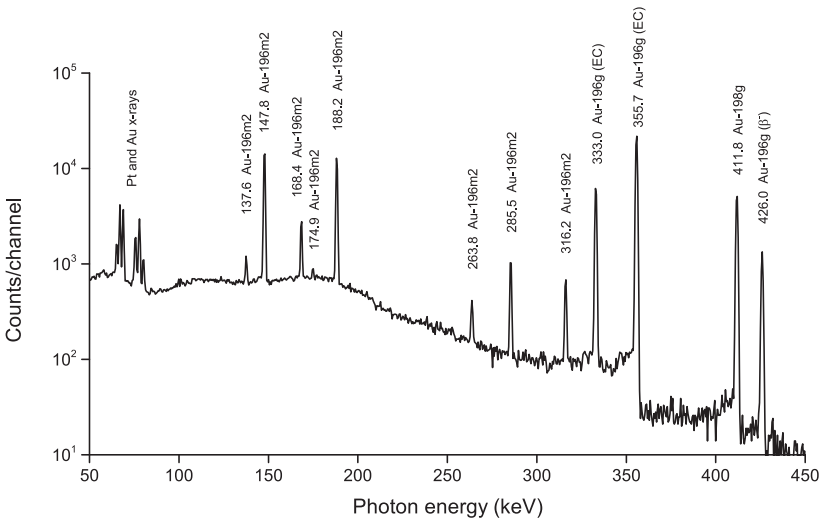

Figure 5. A section of a γ-ray spectrum from a gold foil, sample T63, irradiated with fast neutrons at NIF, counted with a germanium detector for 240 min starting 0.09 d after irradiation, 6.92 cm from the semiconductor face, through a 0.4 g cm^{-2} cadmium attenuator. The γ-lines are identified, all generated by reactions of neutrons with gold.

samples provided internal calibration points to check for drift in the energy calibration over the duration of the measurements, as did the platinum $K\alpha_2$, platinum $K\beta_1$, gold $K\alpha_1$, and gold $K\beta_2$ *x*-ray lines [97]. For standard COAX detectors, spectral data from 50 keV to 2 MeV were collected as time-tagged histograms in 4096 channels; for LEPS counts, data from 20 to 400 keV were collected similarly.

The counting samples were placed in fixtures at well-defined positions ($\pm$0.02 cm), coaxial with the detectors. The detectors and sources were located together in shielded enclosures fabricated from at least 5 cm of lead lined with 1 mm of copper. The activity of the samples was limited so attenuators of precisely machined cadmium or tantalum were often placed between the source and the detector to reduce the coincident summing of the intense platinum and gold *x*-rays with γ-rays emitted by the source. This allowed us to count the samples closer to the detector face than would be otherwise practicable. This was critical in counting samples for half-life measurements since the samples were not moved from their original position through the course of counting even after some of the analyte concentrations had become unobservable due to decay.

In table 3 we summarize details of the construction of the counting sources and how they were counted. Four sources (T61, T98, T63, and T64) were used in measurements of photon energy and relative intensity only, while three sources (T13, T65, and T62) were also counted at regular time-tagged intervals in order to construct decay curves for half-life and absolute photon intensity measurements. Care was taken to assure that the time bases at NIF and in the counting facility were synchronized to within 15 s. The attenuating media were varied across the experiments in order to check the effect of the uncertainty associated with the calculation of half-thicknesses (see below).

Photon spectra were processed with the GAMANAL code [98–100], or by histogram analysis in the event of low statistics [34, 35]. In histogram analysis, the background under the photopeak of interest is established graphically and subtracted from the sum of the data in

Table 3. Information on the seven experimental samples used in the spectrometric measurements related to the decay of $^{196}Au^{m2}$. Irradiation information is given in table 2. Each sample also incorporated a thin aluminum foil, 5.02 cm^2 in area and having a nominal 32.6 mg mass, mounted behind the gold foils. External attenuation is described; the T61 sample was counted both with and without an interposed cadmium foil. The quoted distance is from the middle of the radioactive source to the center of the front surface of the detector semiconductor (not the cryostat). The detector efficiency is that relative to a standard reference NaI(Tl) detector [90].

Sample name	Sample gold mass (g)	Sample area (cm^2)	Attenuation ($g\,cm^{-2}$)	Distance (cm)	Detector efficiency	Brief description
T13	2.5021	4.98	Ta, 0.140	6.97	13%	Followed decay
T65	2.5021	4.98	Cd, 0.402	5.54	20%	Followed decay
T61	2.4328	3.77	Cd, 0.402	10.26	37%	Two detectors and
			Tape, 0.007	8.67	12%	Two attenuators
T98	0.9361	4.73	Tape, 0.007	3.54–6.92	12%–37%	Various detectors
T62	0.9292	4.83	Tape, 0.007	5.78	LEPS	Followed decay
T63	0.9406	4.81	Cd, 0.402	6.92	12%	Four 4 h counts
T64	0.9364	4.79	Tape, 0.007	8.46	30%	Four 4 h counts

a region whose width is taken to be the same as those of nearby peaks with higher counting statistics. GAMANAL requires the prior determination of the spectral peak shape as a function of photon energy for quantification of the peak area, resolution of doublets, and calculation of the peak-energy centroids. The code finds and integrates peaks in the photon spectra over an extrapolated continuum, applies energy and efficiency calibrations, makes a geometric adjustment for the finite extent of the gold foils, and calculates the effects of attenuation by both the sources themselves and by interposed cadmium or tantalum foils as appropriate. The attenuation calculation is based on a set of measured data and a computational model [86, 101]. Although not very important in the current experiment, the code also subtracts the contribution from detector/shield radiation background for each photopeak, measured in a separate long count without a radionuclide source. Uncertainties associated with the resulting γ-ray energy and intensity data are obtained from the statistical weights of the photopeaks and algorithms in the codes, which treat the application of the detector efficiency, photon attenuation, and the geometric correction for the spatial distribution of the sample.

Individual spectra were accumulated over counting intervals of less than the half-lives of the radionuclides of interest. For samples T13, T65, and T62, efficiency-corrected peak areas were tagged with photon energies and elapsed-time information and were sorted into decay curves. For the analysis of simple (single component) decays, the time associated with each photopeak was calculated taking into account the effect of nonlinearity of decay during the finite counting interval. The characteristic time δ, the elapsed time after the start of the data acquisition period associated with the average count rate in the time interval, is given by,

$$\delta = \frac{1}{\lambda} \ln \left[\frac{\lambda \Delta t}{1 - \exp(-\lambda \Delta t)} \right], \tag{1}$$

where Δt is the length (real time) of the count interval and λ is the decay constant [102]. When λ is not known, the decay curve analysis becomes iterative and δ is recalculated and applied to the input data after each redetermination of the half-life until λ converges. Decay

curve analyses were performed with a nonlinear least squares code [102, 103]. For half-life determinations, the decay of each sample was followed for at least 10 d during which time the position of the sample relative to the detector was fixed.

In the decays of both ^{196}Au^{m2} and ^{196}Au^{g}, photopeaks due to the summing of the two strongest γ-lines were observed ($148 + 188 = 336$ keV and $333 + 356 = 689$ keV, respectively), with apparent intensities far in excess of those reported for the direct decays [27]. The apparent intensity of the 336 keV line relative to that of the 188 keV line emitted in the IT decay of ^{196}Au^{m2} was less than 0.9% in all cases. The apparent intensity of the 689 keV line relative to that of the 333 keV line emitted in the EC decay of ^{196}Au^{g} was less than 1.3% in all cases. The sum lines at 336 and 689 keV were found to decay with the same apparent half-lives as ^{196}Au^{m2} and ^{196}Au^{g}, respectively, indicating that coincident summing is far more important than is random summing in these experiments [104–106]. The potential effects of summing in the data analysis presented here were ignored.

GAMANAL calculates attenuation by interpolation from a table of photon cross sections for a variety of materials [86]. The attenuation from 7 mg cm^{-2} of plastic tape is trivially small at all photon energies reported in these experiments, so water was substituted in the attenuation calculation for the chemically undefined plastic. Both tantalum and cadmium are adequately described in GAMANAL, resulting in half-thicknesses with uncertainties of less than 2% [107]. GAMANAL does not have $Z = 79$ in its attenuation table, so the code constructs attenuation parameters from a linear combination of the data for $Z = 78$ and $Z = 82$. This results in an error in the calculation of the half-thicknesses of gold as a function of energy that can be significant compared to the uncertainties derived from the counting statistics, particularly in the vicinity of the K edges [86]. Corrections required to compensate for the improper application of the attenuation due to gold were performed by hand after the GAMANAL calculations were complete.

4. Results

The decay properties of ^{196}Au^{m2} that were determined in γ-ray spectrometry experiments are outlined in the following subsections. As a byproduct, some of the characteristics of the decays of other radioisotopes produced in the irradiation of ^{197}Au with fast neutrons at NIF were also measured. When more than one measurement of a given quantity was made, the weighted average is presented; since the individual measurements often had significantly different statistical weights, in most cases this was more appropriate than the calculation of the standard deviation of the mean. Reported weighted average values are calculated using the standard method while the uncertainty is dependent on internal or external consistencies within the given set of measurements. The weighted average ($\bar{x}$) for n measurements of x ($x_1 \pm \Delta x_1$, $x_2 \pm \Delta x_2$, … $x_n \pm \Delta x_n$) is calculated as:

$$\bar{x} = \frac{\sum \frac{x_i}{\Delta x_i^2}}{\sum \frac{1}{\Delta x_i^2}}. \tag{2}$$

The uncertainty corresponding to $\bar{x}$, ($\Delta\bar{x}$), is given as the larger of:

$$\Delta\bar{x} = \sqrt{\frac{1}{\sum \frac{1}{\Delta x_i^2}}} \tag{3}$$

or

$$\Delta\bar{x} = \sqrt{\frac{1}{\sum\frac{1}{\Delta x_i^2}}\sum\left[\left(\frac{1}{\Delta x_i^2}\right)\frac{(\bar{x} - x_i)^2}{(n-1)}\right]}. \tag{4}$$

If the measured data set is consistent, $\Delta\bar{x}$ is represented by equation (3) (e.g. table 5) while inconsistencies result in the use of the $\Delta\bar{x}$ as defined in equation (4) (e.g. table 1). All errors are reported at the one-sigma limit. The treatment of statistical and systematic uncertainties is discussed later in the text.

4.1. Measurement of the energies of the γ-rays emitted in $^{196}Au^{m2}$ decay

The γ-ray spectra obtained in the experiments were stored in the form of a histogram. The centroid of a photopeak was calculated from the data in an energy window, both an average channel number weighted by the counts in each channel in excess of the continuum, and a channel number associated with the fit of the GAMANAL peak shape. The statistical uncertainty of each peak channel derived from the histogram is attached to the average of the two values, which is converted to an energy through the use of calibration sources. The energy calibrations of the counting electronics associated with the detectors were stable over extended counting intervals, with peak centroids shifting by less than 0.1 channel over several weeks as determined through surveillance of the derived energies of the photopeaks arising in the decays of long-lived radionuclides in the sources, mainly $^{196}Au^{g}$ and $^{198}Au^{g}$. There can be complications in energy calibrations if photopeaks are resolved from incompletely separated multiplets, or if the continuum cannot be established accurately due to an inordinate number of nearby peaks. Fortunately, neither is applicable to this work for photopeaks more energetic than the gold and platinum *K x*-rays. Another potential complication arises in the subtraction of detector background. For the γ-rays emitted in the decays of the radionuclides in the sources, only the 84.7 keV line has a significant interference from background, which in this case comes from photons emitted in the decays of members of the ^{232}Th decay chain [108].

For the measurements presented below, data were used from all seven samples listed in table 3, taken within 30 h (three half-lives of $^{196}Au^{m2}$) of the relevant irradiation time. Exceptions are the values presented for the 84.7 keV photon, where only the first 10 h of counting were used and data taken on detectors with high ^{232}Th backgrounds were excluded. A weighted average of the energy of each photopeak in each count of each sample was generated. The statistical uncertainties on these values are quite small, and in most cases are completely overwhelmed by the systematic uncertainty that arises in energy calibrations, 0.04–0.06 keV over the relevant portions of the γ-ray spectra.

In table 4 the determinations of the energies of the photons emitted in the decays of $^{196}Au^{m2}$, $^{196}Au^{g}$, $^{198}Au^{g}$, and ^{24}Na are presented. The last three radionuclides were included as method validation. Photon-energy values from the literature are included as a comparison. The values given in [109] for two of the γ-transitions in the decay of $^{196}Au^{m2}$ were derived from electron spectroscopy and are probably the most precise. The best values for the energies of the other γ-rays emitted in the decay of $^{196}Au^{m2}$ were reported by Wapstra [41], but were shifted upwards by 40 eV in a subsequent data evaluation to account for changes in calibration [27]. For photons emitted in the decay of $^{196}Au^{m2}$, it was found that the values derived from this work are in substantial agreement with the literature, though they offer no significant improvement. For photons emitted in the decays of $^{198}Au^{g}$ and ^{24}Na, the data derived from this work reproduce the more precise literature values, although the literature data for the 1369 keV photon emitted in the decay of ^{24}Na are somewhat discrepant. It was found that the

Table 4. Reported energies (in keV) of γ-rays emitted in the decays of $^{196}Au^{m2}$, $^{196}Au^{g}$, $^{198}Au^{g}$, and ^{24}Na. One-sigma uncertainties are given in parentheses, relative to the last significant digit(s) of the experimental values.

	γ-ray energy (keV)					
Isotope	[27]	[41]	[82]	[109]	[110]	This work
$^{196}Au^{m2}$	84.66(2)	84.62(2)	84.6			84.69(5)
	137.69(3)	137.65(3)	137.7			137.65(5)
	147.81(2)	147.77(2)	147.8	147.773(16)	147.9	147.78(5)
	168.37(2)	168.33(2)	168.3			168.35(5)
	174.91(2)	174.87(2)	174.9	174.867(21)	174.9	174.93(7)
	188.27(3)	188.23(3)	188.2		188.4	188.24(5)
	264.0(5)	264.0(5)				263.76(5)
	285.49(7)	285.45(7)				285.48(5)
	316.19(5)	316.15(5)				316.19(5)
Isotope	[27]	[55]	[111]			This work
$^{196}Au^{g}$	326.2(4)		326.2(4)			326.38(8)
	333.03(5)	333.03(5)	333.0			333.03(5)
	355.73(5)	355.73(5)	355.7			355.73(5)
	426.0(1)		426.1			425.99(5)
	521.4(2)		521.4(2)			521.18(6)
	759.1(3)		759.1(3)			758.32(6)
	1091.4(2)	1091.33(30)	1091.4(2)			1091.30(6)
Isotope	[89]	[112]	[113, 114]	[115]		This work
$^{198}Au^{g}$	411.795(9)	411.794(8)	411.8044(2)	411.8020(2)		411.82(5)
		675.871(18)	675.8874(7)	675.8836(7)		675.90(5)
Isotope	[89]	[106]	[116]	[115]		This work
^{24}Na	1368.568(44)	1368.55	1368.672(5)	1368.626(5)		1368.54(6)

data from these irradiations provide a significant improvement over values reported in the literature for the energies of the minor transitions in the decay of 6.2 d $^{196}Au^{g}$, and are in substantial agreement, with the exception of the γ-line at 758 keV, where the data disagree by 0.8 keV. This difference was first noticed in spectra of high-yield debris collections, but the possibility of interference from some undefined component of the radiochemically complicated samples could not be excluded. The activated gold spectra are less complicated (see figure 5), and the discrepancy relative to the literature is reproduced.

4.2. Measurement of the half-life of the decay of $^{196}Au^{m2}$

As described in section 3.2, decay curves were constructed for each of the six most intense γ-lines associated with the decay of $^{196}Au^{m2}$. For the three samples whose decay was followed (T13, T65, and T62), a total of 18 separate determinations of the half-life were performed. Four representative decay curves are shown in figure 6. Calculation of a half-life from γ-spectrometric data can suffer from inaccuracies that were minimized or eliminated based on the experimental setup. The samples were placed at fixed locations relative to the detector and were not moved for the duration of the measurements, eliminating uncertainties associated with detector efficiency calibration. As analyte signals decay with time, any error in the subtraction of the continuum has a strong effect on the residual photopeak areas and,

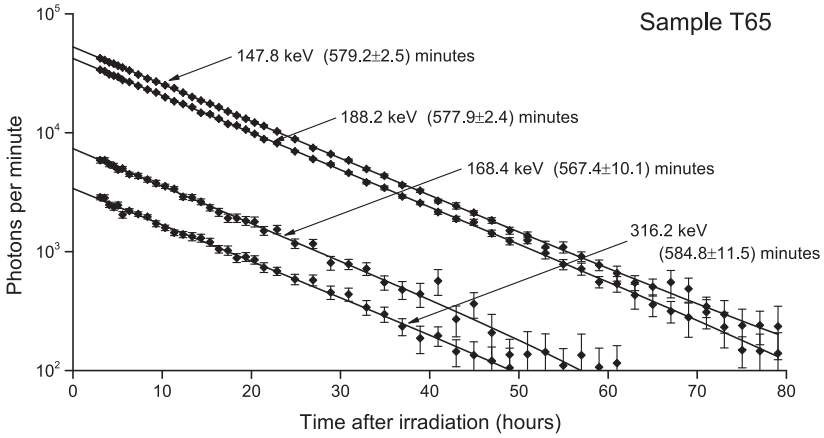

Figure 6. Four representative decay curves of photons arising in the decay of $^{196}Au^{m2}$, sample T65. Only the first 80 h of data are shown. Vertical one-sigma error bars on the data points are smaller than the size of the markers unless explicitly shown.

consequently, the calculation of the half-life. The structure of the continuum under the $^{196}Au^{m2}$ photopeaks arises primarily from the decay of longer-lived $^{196}Au^{g}$, so the shape and magnitude of the continuum change slowly with time. The uncertainty associated with subtraction of the continuum is not strongly affected by the gross count rate of the sample over the course of the measurements [106], and is assumed to be handled properly in the GAMANAL analysis. The electronic dead time associated with data collection was never greater than 1.0%, minimizing potential time-base issues associated with real-time/live-time calculations. Also, by using three different attenuators and three different detectors (including a LEPS detector), any overall bias in the measurements was minimized.

The decay curve associated with each photopeak was treated as a simple (i.e. single-component) decay. In table 5 the 18 values of the half-life of $^{196}Au^{m2}$ that were obtained in these experiments are listed. The weighted-average half-life is 9.603 h, with a one-sigma uncertainty of 0.23%. The $^{196}Au^{m2}$ half-life could also be extracted from the ingrowth of the strongest γ-lines emitted in the decay of the $^{196}Au^{g}$ decay daughter (see section 4.4). Those results were consistent with the direct measurements in table 5, but are of much lower statistical value and were not included in the calculation of the average.

1n addition to $^{196}Au^{m2}$, half-lives for $^{198}Au^{g}$ and ^{24}Na were also extracted from the counting data. This was done as a check of the method, although counting was not optimized for $^{198}Au^{g}$, and the γ-ray activity due to decays of ^{24}Na had lower counting statistics. Neither radionuclide was observed in counts of sample T62 where a LEPS detector was used to follow the decays. The values obtained for the decay half-lives of $^{198}Au^{g}$, ^{24}Na, and $^{196}Au^{m2}$ are presented in table 6, along with examples of similar measurements from the indicated literature. The measured half-lives of $^{198}Au^{g}$ and ^{24}Na are consistent with the more precise literature values. The value for the half-life of $^{196}Au^{m2}$ obtained from this work is consistent with the literature, but with a smaller associated uncertainty (the value in [76] was given without an error bar).

4.3. The relative intensities of the γ-rays emitted in the decays of gold isotopes

In the measurements of relative γ-ray intensities, particularly those involving low-energy photons, issues of detector efficiency calibration and attenuating media are paramount. The

Table 5. Determinations of the half-life of $^{196}Au^{m2}$ from decay-curve analyses of the six strongest γ-ray transitions observed in the three indicated counting samples.

Sample	Photon energy (keV)	Half-life (min)
T13	137.6	523.5 ± 132.4
	147.8	569.5 ± 8.0
	168.4	585.0 ± 46.1
	188.2	567.0 ± 8.8
	285.5	592.7 ± 35.1
	316.2	514.6 ± 39.6
T62	137.6	568.0 ± 36.0
	147.8	570.9 ± 2.8
	168.4	592.6 ± 16.7
	188.2	579.6 ± 4.3
	285.5	574.7 ± 19.9
	316.2	539.3 ± 26.7
T65	137.6	577.7 ± 38.6
	147.8	579.2 ± 2.5
	168.4	567.4 ± 10.1
	188.2	577.9 ± 2.4
	285.5	574.3 ± 8.5
	316.2	584.8 ± 11.5
	Weighted average	576.2 ± 1.3

Table 6. Comparison of measured half-lives from this work with values from the indicated literature, for decays of $^{198}Au^{g}$, ^{24}Na, and $^{196}Au^{m2}$.

Isotope or sample ID	Half-life	References
$^{198}Au^{g}$	2.6946 ± 0.0010 d	[117]
	2.6943 ± 0.0008 d	[118]
	2.6966 ± 0.0007 d	[119]
	2.6956 ± 0.0003 d	[120]
	2.6947 ± 0.0006 d	[121]
	2.6949 ± 0.0009 d	[122]
T13	2.7031 ± 0.0121 d	This work
T65	2.6883 ± 0.0049 d	This work
^{24}Na	14.959 ± 0.010 h	[123]
	15.09 ± 0.06 h	[124]
	14.9654 ± 0.0041 h	[118]
	14.9512 ± 0.0032 h	[120]
T13	15.18 ± 0.58 h	This work
T65	14.92 ± 0.12 h	This work
$^{196}Au^{m2}$	600 ± 30 min	[50]
	588 ± 18 min	[51]
	570 ± 18 min	[52]
	582 ± 6 min	[74]
	624 ± 60 min	[75]
	576 min	[76]
	567 ± 12 min	[40]
	576.2 ± 1.3 min	This work (average)

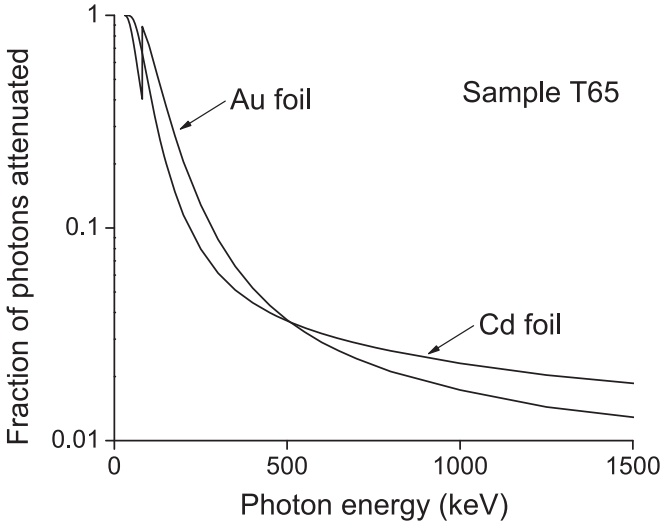

Figure 7. Attenuation of photons relevant to sample T65. The fraction of emitted photons attenuated by 402 mg cm^{-2} of cadmium is given, as is that associated with $\frac{1}{2}$ the thickness of the 502 mg cm^{-2} gold foil, an approximation of self-attenuation.

effects of errors in calibration were minimized by using several different detectors in the course of the experiments. The systematic uncertainty of 1%–2%, from the uncertainties of the decay rates of the radionuclides in the sources used in the calibration of the detectors, does not apply to the reported ratios of γ-ray intensities.

The half-thicknesses used in the attenuation correction have uncertainties of 2% [107], which translates to an uncertainty in the fraction of photons attenuated ($F(\gamma)$) through the expression,

$$F(\gamma) = 1 - 2^{-T/h(\gamma)}, \tag{5}$$

where T is the areal density of the attenuator and $h(\gamma)$ is the half thickness. In figure 7 we show the attenuation associated with the media for the counts of sample T65, the 402 mg cm^{-2} cadmium external foil and half the thickness of the 502 mg cm^{-2} activated gold foil. GAMANAL performs a more accurate incremental calculation for self-attenuation by the source, but this was approximated for the purpose of discussion by displaying the attenuation by half of the target-foil thickness in figure 7. For photons with energies $\geqslant$300 keV, a 2% uncertainty on the half-thickness has a small effect on the uncertainty of the γ-ray intensity measurements, $[1 - F(\gamma)]_{\mathrm{Au}} \times [1 - F(\gamma)]_{\mathrm{Cd}}$ for sample T65. At lower energies, the uncertainty becomes more important, surpassing 2% for energies below 150 keV.

Through the use of intensity ratios, the attenuation uncertainty caused by the systematic uncertainty in the half-thickness partially cancels for photopeaks that are proximate in energy. The GAMANAL calculation of photon intensities propagates an attenuation uncertainty such that individual intensity ratios based on the weighted averages of several measurements will have associated error bars that are too small, particularly for ratios involving low-energy transitions. The systematic uncertainty due to attenuation is reapplied after the averages are calculated. Traditionally, relative photon intensities are based on the transition of highest intensity, but in this case the 148 keV transition is significantly more attenuated than is the slightly less intense 188 keV transition, resulting in a larger absolute uncertainty in intensity.

Therefore, the intensity ratio calculations presented here were based on the 188 keV photopeak.

As a check of the method, intensity ratios were also measured for the photons emitted in decays of $^{196}Au^{g}$ and $^{198}Au^{g}$, relative to their 356 keV and 412 keV photopeaks, respectively. In $^{196}Au^{g}$ decay, most of the γ-ray intensity is three γ-lines (333, 356, and 426 keV), but lines of lower intensity associated with the EC branch were also observed. In $^{198}Au^{g}$ decay, only one intensity ratio could be measured, so the entries for those particular sources are omitted from the table when both photopeaks were not observed. Similar to the treatment of detector efficiency calibration, the parameters of attenuation were varied across the set of experiments to attempt to compensate for any errors inherent in the attenuation calculation. Perhaps more importantly, three different thicknesses of gold foils were used as targets in the irradiations to assess the GAMANAL calculation of self-attenuation by the source medium.

In table 7 the average values of the photon-intensity ratios obtained from each of the seven experimental samples are reported. Sample T61 has two entries because it was counted both with and without an interposed cadmium foil. For samples T63, T64, T98, and T61, the intensity ratios were obtained from individual spectra and weighted averages were obtained for each sample. For samples T13, T62, and T65, where the data were time-tagged and used to construct decay curves, the intensity ratios were derived from decay-curve analyses in which the half-lives were held constant. The final weighted averages were derived from the data values given in table 7 for each individual sample, when measured.

As discussed above, the weighted-average values of the intensity ratios given in table 7 have associated uncertainties that are underestimated, and require application of the systematic error arising from the attenuation correction. This uncertainty is small for the higher-energy transitions involved in the decays of $^{196}Au^{g}$ and $^{198}Au^{g}$, but is significant for the lower-energy photons emitted in the decay of $^{196}Au^{m2}$. The weighted average of each intensity ratio is most strongly influenced by the entry for sample T65, except the average value for the 84.7/188.2 keV ratio, which is most strongly influenced by the sources produced from thin gold foils. Therefore, with that sole exception, the systematic uncertainties derived from the attenuation data for sample T65 (depicted in figure 7) were propagated with the intensity ratios given in table 7 to generate the final intensity ratios, which are reported in table 8. For the 84.7/188.2 keV ratio, the uncertainties associated with self-attenuation by a thin gold target were propagated without additional attenuation. Table 8 also includes comparative data from the indicated literature. The literature data for $^{196}Au^{m2}$, which have historically been based on a 148 keV photon intensity of 5.00 [38, 41], have been reformulated to match the basis presented here, where the 188 keV intensity is 1.00.

The data obtained in this work for the relative intensities of photons emitted in decays of $^{196}Au^{g}$ and $^{198}Au^{g}$ are consistent with those found in the literature, with the data reported here for $^{196}Au^{g}$ decay constituting an improvement. A substantial discrepancy was measured between the data for $^{196}Au^{m2}$ decay and that reported in the literature as expected (see section 1). The results of the present work are in closer agreement with the experimental data from 1967 [41] than with the evaluated data from 2007 [27].

4.4. Absolute normalization of the intensities of photons emitted in the decay of $^{196}Au^{m2}$

The parent-daughter connection between the radioactive decays of $^{196}Au^{m2}$ and $^{196}Au^{g}$ provides the means for determining an absolute normalization of the intensities of the γ-rays emitted in $^{196}Au^{m2}$ decay. This results from an established radiochemical method, involving the measurement of the decay of $^{196}Au^{g}$ shortly after irradiation of the target and observing a

Table 7. γ-ray intensity ratios for photons emitted in the decays of gold isotopes produced in the reaction of ^{197}Au with fast neutrons, summarized for individual experimental samples. The abbreviation n.m. is not measured due to the absence of observed intensity of the photon transition in the numerator. The description field is a mnemonic that refers to the sample characteristics given in more detail in table 3. The weighted averages do not incorporate the systematic uncertainty due to the attenuation of photons, which was applied to the final data that are reported in table 8. Uncertainties are one-sigma.

γ-ray intensity ratios for ^{196}Au^{m2}									
Sample ID	T63	T64	T98	T61	T61	T13	T62	T65	Weighted average
Description	Thin gold, cadmium	Thin gold, tape	Thin gold, tape	Thick gold, tape	Thick gold, cadmium	Thick gold, tantalum	Thin gold, tape	Thick gold, cadmium	
84.7 keV/188.2 keV	0.0168 ± 0.0153	0.0220 ± 0.0038	n.m.	0.0829 ± 0.0449	n.m.	n.m.	0.01332 ± 0.00215	0.01201 ± 0.00742	0.01535 ± 0.00228
137.6 keV/188.2 keV	0.04413 ± 0.00328	0.04737 ± 0.00281	0.04241 ± 0.00442	0.04890 ± 0.00645	0.04823 ± 0.01201	0.05186 ± 0.00671	0.04511 ± 0.00176	0.04456 ± 0.00175	0.04525 ± 0.00102
147.8 keV/188.2 keV	1.2405 ± 0.0127	1.2953 ± 0.0100	1.2643 ± 0.0148	1.3145 ± 0.0194	1.3224 ± 0.0278	1.2398 ± 0.0178	1.2394 ± 0.0076	1.2616 ± 0.0054	1.2614 ± 0.0081
168.4 keV/188.2 keV	0.1720 ± 0.0046	0.1772 ± 0.0037	0.1751 ± 0.0069	0.1763 ± 0.0084	0.1683 ± 0.0084	0.1842 ± 0.0081	0.1703 ± 0.0030	0.1736 ± 0.0020	0.1736 ± 0.0014
174.9 keV/188.2 keV	0.01210 ± 0.00247	0.01422 ± 0.00254	0.01421 ± 0.00469	0.01518 ± 0.00793	n.m.	n.m.	0.01138 ± 0.00185	0.01299 ± 0.00120	0.01274 ± 0.00086
263.8 keV/188.2 keV	0.02940 ± 0.00229	0.03084 ± 0.00188	0.02897 ± 0.00306	0.02794 ± 0.00341	0.02788 ± 0.00388	0.03335 ± 0.00342	0.02738 ± 0.00190	0.03094 ± 0.00087	0.03021 ± 0.00065
285.5 keV/188.2 keV	0.11687 ± 0.00258	0.12239 ± 0.00247	0.11649 ± 0.00355	0.10667 ± 0.00466	0.11421 ± 0.00524	0.11295 ± 0.00407	0.10881 ± 0.00268	0.11706 ± 0.00116	0.11623 ± 0.00140
316.2 keV/188.2 keV	0.0808 ± 0.0026	0.08675 ± 0.00262	0.08065 ± 0.00386	0.07471 ± 0.00469	0.07349 ± 0.00483	0.07930 ± 0.00380	0.07435 ± 0.00248	0.08131 ± 0.00102	0.08050 ± 0.00119
γ-ray intensity ratios for ^{196}Au^{g}									
Sample ID	T63	T64	T98	T61	T61	T13	T62	T65	Weighted average
Description	Thin gold, cadmium	Thin gold, tape	Thin gold, tape	Thick gold, tape	Thick gold, cadmium	Thick gold, tantalum	Thin gold, tape	Thick gold, cadmium	
326.4 keV/355.7 keV	0.00174 ± 0.00036	0.00104 ± 0.00030	n.m.	n.m.	n.m.	n.m.	n.m.	0.00124 ± 0.00012	0.00126 ± 0.00012
333.0 keV/355.7 keV	0.26587 ± 0.00154	0.26320 ± 0.00135	0.26493 ± 0.00122	0.26665 ± 0.00182	0.26720 ± 0.00271	0.26801 ± 0.00534	0.26717 ± 0.00344	0.26301 ± 0.00050	0.26378 ± 0.00050
426.0 keV/355.7 keV	0.07422 ± 0.00076	0.07583 ± 0.00073	0.07482 ± 0.00055	0.07423 ± 0.00087	0.07358 ± 0.00130	n.m.	n.m.	0.07400 ± 0.00024	0.07425 ± 0.00023
521.2 keV/355.7 keV	n.m.	0.00040 ± 0.00019	0.00057 ± 0.00010	0.00064 ± 0.00021	0.00049 ± 0.00025	n.m.	n.m.	0.00052 ± 0.00005	0.000525 ± 0.000043

Table 7. (Continued.)

γ-ray intensity ratios for $^{196}Au^{m2}$									
Sample ID Description	T63 Thin gold, cadmium	T64 Thin gold, tape	T98 Thin gold, tape	T61 Thick gold, tape	T61 Thick gold, cadmium	T13 Thick gold, tantalum	T62 Thin gold, tape	T65 Thick gold, cadmium	Weighted average
758.3 keV/355.7 keV	n.m.	0.00080 ± 0.00042	0.00052 ± 0.00010	n.m.	n.m.	n.m.	n.m.	0.00055 ± 0.00004	0.000547 ± 0.000038
1091.3 keV/355.7keV	0.00277 ± 0.00055	0.00223 ± 0.00037	0.00189 ± 0.00016	0.00186 ± 0.00034	0.00254 ± 0.00096	n.m.	n.m.	0.00189 ± 0.00007	0.001912 ± 0.000062
γ-ray intensity ratios for $^{198}Au^{g}$									
Sample ID	T63	T64	T98	T61					Weighted average
Description	Thin gold, cadmium	Thin gold, tape	Thin gold, tape	Thick gold, tape					
675.9 keV/411.8 KeV	0.00923 ± 0.00097	0.00891 ± 0.00102	0.00728 ± 0.00118	0.00912 ± 0.000942					0.00873 ± 0.00055

Table 8. As reported γ-ray intensity ratios and a comparison of the present work with relevant results from the literature. Uncertainties are one-sigma.

Isotope	Photon energies	References				
		[41]	[27]			This work
$^{196}Au^{m2}$	84.7 keV/188.2 keV	$\leqslant$ 0.023	0.0101 ± 0.0004			0.01535 ± 0.00230
	137.6 keV/188.2 keV	0.0341 ± 0.0115	0.0435 ± 0.0146			0.04525 ± 0.00115
	147.8 keV/188.2 keV	1.136 ± 0.052	1.449 ± 0.050			1.2614 ± 0.0147
	168.4 keV/188.2 keV	0.205 ± 0.015	0.2609 ± 0.0171			0.1736 ± 0.0018
	174.9 keV/188.2 keV		0.01461 ± 0.00057			0.01274 ± 0.00086
	263.8 keV/188.2 keV		0.0435 ± 0.0146			0.03021 ± 0.00070
	285.5 keV/188.2 keV	0.116 ± 0.013	0.1478 ± 0.0154			0.11623 ± 0.00172
	316.2 keV/188.2 keV	0.077 ± 0.008	0.0986 ± 0.0094			0.08050 ± 0.00141
		[55]	[125]	[57]	[111]	This work
$^{196}Au^{g}$	326.4 keV/355.7 keV				0.00113 ± 0.00025	0.00126 ± 0.00012
	333.0 keV/355.7 keV	0.28	0.270 ± 0.010	0.27	0.263 ± 0.006	0.26378 ± 0.00073
	426.0 keV/355.7 keV		0.060 ± 0.010	0.057 ± 0.010	0.0762 ± 0.0010	0.07425 ± 0.00030
	521.2 keV/355.7 keV		0.00050 ± 0.00015	0.00073 ± 0.00015	0.000447 ± 0.000010	0.000525 ± 0.000043
	758.3 keV/355.7 keV		0.00040 ± 0.00005	0.00050 ± 0.00007	0.000510 ± 0.000020	0.000547 ± 0.000038
	1091.3 keV/355.7 keV	0.0017 ± 0.0004	0.0024 ± 0.0001	0.0020 ± 0.0001	0.00171 ± 0.00007	0.001912 ± 0.000063
		[126]	[127]	[128]	[129]	This work
$^{198}Au^{g}$	675.9 keV/411.8 keV	0.00820 ± 0.00056	0.0097 ± 0.0011	0.00841 ± 0.00003	0.00846 ± 0.00009	0.00873 ± 0.00055

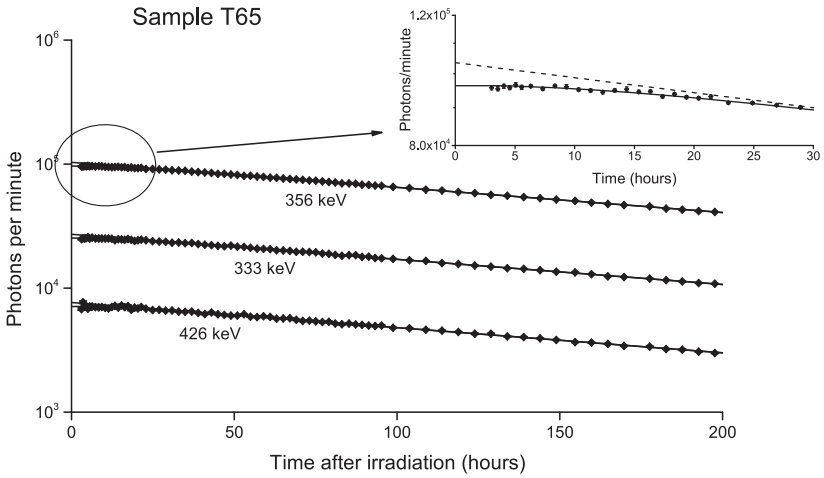

Figure 8. Three decay curves from the decay of $^{196}Au^{g}$ in sample T65. Vertical one-sigma error bars on the data points are smaller than the size of the markers. Early-time data for the strongest γ-transition is expanded in the frame at the upper right. It clearly shows that the data points and the associated fit (solid line) deviate from hypothetical single-component behavior extrapolated from late counts (dashed line), demonstrating the effect of decay of the $^{196}Au^{m2}$ parent on the concentration of the $^{196}Au^{g}$ daughter.

deviation from simple (single-component) radioactive decay caused by ingrowth of the ground state from the decays of the metastable state.

The equation that describes the activity of a daughter nuclide (A_d) as a function of time is,

$$A_d(t) = \frac{\lambda_d A_p^o}{(\lambda_d - \lambda_p)}(\exp(-\lambda_p t) - \exp(-\lambda_d t)) + A_d^o \exp(-\lambda_d t), \tag{6}$$

where A_d^o and A_p^o are the initial activities of the daughter and parent nuclides, respectively, t is the post-irradiation time associated with the measurement of A_d, and λ_d and λ_p and the decay constants of the daughter and parent nuclide, respectively, and are equal to ln(2) divided by the appropriate half-life. Equation (6) is applied to the case where A_p is the decay rate of $^{196}Au^{m2}$ and A_d is that of $^{196}Au^{g}$. Since the counting of NIF samples did not begin until after 90 min post irradiation, there is no measurable deviation from the behavior described by equation (6) due to the independent production of the 8.2 s $^{196}Au^{m1}$ intermediate state. If the half-lives of the two species are known accurately, the functional form of the decay of the daughter activity depends only on A_d^o and A_p^o, and puts the decay of $^{196}Au^{m2}$ on the well-characterized intensity basis of the radiations emitted in the decay of $^{196}Au^{g}$. Figure 8 is a plot of the experimental data for sample T65, depicting the intensities of the three strongest γ-lines emitted in the decay of $^{196}Au^{g}$ as a function of time. The data for the 356 keV line at early times are expanded in the frame at the upper-right of the figure, showing the deviation from single-component decay of $^{196}Au^{g}$ caused by the precursor decay of $^{196}Au^{m2}$. The statistical significance of the difference between single-component decay (dashed line) and the functional fit of equation (6) to the data (solid line) can be improved with stronger sources, but more importantly by counting the sources soon after the end of irradiation.

The time-dependent intensities of the strongest γ-lines emitted in the decay of $^{196}Au^{g}$ in the three samples whose decays were followed were fit with the functional form of equation (6). The values of λ were held constant in the calculation, and were computed from

Table 9. Calculation of the initial activity ratio (A_p^o/A_d^o) of $^{196}Au^{m2}/^{196}Au^g$ arising from decay curve analyses of the strongest γ-rays emitted in the decay of $^{196}Au^g$ in the indicated samples. The weighted average of the eight determinations is given, and is converted to an isomer ratio through the application of the decay constants. Uncertainties are one-sigma.

Sample ID	Photon energy (keV)	Initial activity $^{196}Au^{m2}$ (counts min^{-1})	Initial activity $^{196}Au^g$ (counts min^{-1})	Activity ratio
T13	333.0	4720 ± 1330	5099.2 ± 88.9	0.926 ± 0.262
	355.7	19780 ± 2750	19026 ± 184	1.040 ± 0.070
	426.0	2832 ± 733	1291.3 ± 48.6	2.193 ± 0.574
T62	333.0	12590 ± 1880	10571 ± 122	1.191 ± 0.178
	355.7	46120 ± 3500	39567 ± 226	1.166 ± 0.089
T65	333.0	28820 ± 1760	25291 ± 113	1.139 ± 0.070
	355.7	108000 ± 3730	96363 ± 236	1.121 ± 0.039
	426.0	8170 ± 980	7107 ± 63	1.150 ± 0.138
			Weighted average	1.119 ± 0.028
			Isomer ratio (atom ratio)	0.0731 ± 0.0019

Table 10. Absolute normalization of the intensity of the 188.2 keV γ-ray emitted in the decay of $^{196}Au^{m2}$ for each of the indicated samples. The decay rate of $^{196}Au^{m2}$ derives from decay curve analyses of the γ-ray transitions emitted in $^{196}Au^g$ decay, corrected for their absolute branching ratios (tables 8 and 11). Uncertainties are one-sigma.

Sample ID	Decay rate of $^{196}Au^{m2}$ (disintegrations min^{-1})	Intensity of 188.2 keV line (γ min^{-1})	Decay branch
T13	23480 ± 2710	8073 ± 115	0.3438 ± 0.0400
T62	53460 ± 3670	16462 ± 179	0.3080 ± 0.0214
T65	124600 ± 3900	42618 ± 429	0.3420 ± 0.0112
		Weighted average	0.3352 ± 0.0097

half-lives of 9.603 h (see section 4.2) and 6.167 d (see table 11) for the decays of $^{196}Au^{m2}$ and $^{196}Au^g$, respectively. Since the decay of sample T62 was followed with a LEPS detector, the 426 keV γ-ray was not observed in that sample, allowing a total of eight values of A_p^o/A_d^o, which are reported in table 9.

The weighted average of the eight measurements of the initial activity ratio of $^{196}Au^{m2}/^{196}Au^g$ is 1.119 ± 0.028. Since the activity of a radionuclide is related to the number of atoms in the sample by $A = \lambda N$, the initial atom ratio of $^{196}Au^{m2}/^{196}Au^g$ is 0.0731 ± 0.0019 (± 2.6%). Since in an instantaneous irradiation the post-irradiation atom ratio is equal to the ratio of the production cross sections (no saturation effects) [87], the isomer ratio is also 0.0731. Uncertainties in efficiency calibration and attenuation do not apply because both initial activities were obtained from single γ-ray lines.

The counts min^{-1} values given in table 9 for $^{196}Au^{m2}$ can be converted to absolute disintegrations min^{-1} through the application of the photon intensity of the transition in $^{196}Au^g$, the observable from which the $^{196}Au^{m2}$ initial activities were derived through decay-curve analysis. The weighted average of the absolute decay rate of $^{196}Au^{m2}$ at end of irradiation is given in table 10 for each sample, using relative intensity data for $^{196}Au^g$ from

Table 11. Nuclear decay data used for calculations of reaction product atom ratios, obtained from [81] unless otherwise noted in the text. Uncertainties (one-sigma) of the last significant digit(s) are given in parentheses.

Nuclide	Half-life	Normalization	Photon energy (keV)	Relative intensity
^{24}Na	14.9590(12) h	1	1368.6	1
^{195}Au	186.09(5) d	0.109(6)	98.9	1.00(5)
^{196}Au^{g} (EC)	6.167(1) d	0.869(9)	333.0	0.263(6)
			355.7	1
			1091.4	0.00171(7)
^{196}Au^{g} (β^{-})	6.167(1) d	0.066(3)	426.0	1
^{198}Au^{g}	2.6947(3) d	0.9558(12)	411.8	1
^{198}Au^{m}	2.272(16) d	0.77(1)	97.2	0.90(4)
			180.3	0.84(5)
			204.1	0.65(4)
			214.9	1
^{197}Pt^{m}	95.4(2) min	1	279.0	0.024(3)
			346.5	0.111(3)
^{197}Pt^{g}	19.8915(19) h	1	191.5	0.037(4)
^{194}Ir	19.15(3) h	1.00(5)	328.5	0.93(5)
			482.6	0.97(5)

table 8 and the absolute normalization from table 11 (below). The initial activities of the 188.2 keV γ-ray resulting from single-component decay curve analyses are also given in table 10. In this case, the systematic uncertainties associated with the efficiency calibration of the detector and the attenuation of the 188 keV γ-ray are relevant, and are components of the quoted uncertainties. The decay branch resulting in the emission of 188 keV photons is the ratio of the intensity of the γ-ray transition to the absolute decay rate of the radioisotope, derived in table 10 for the three indicated samples. These independent analyses result in similar values for the decay branch, giving a weighted average of 0.3352 ± 0.0097 ($\pm$ 2.9%). The decay of ^{196}Au^{m2} results in 188 keV photons 33.5% of the time, and the data in table 8 for the relative intensities of γ-rays arising in ^{196}Au^{m2} decay may then be normalized to this value.

4.5. Production of other radioisotopes in the reactions of fast neutrons with ^{197}Au

Thus far, this work has focused on the gold isotopes ^{196}Au^{m2}, ^{196}Au^{g}, and ^{198}Au^{g}, the dominant activities produced in NIF irradiations of ^{197}Au. Other reaction products formed with lower probabilities are sensitive to different portions of the neutron spectrum (see section 5.4). The γ-ray spectra obtained from samples T65, T98, and T62 were examined to either quantify or establish limits for the concentrations of these products, using the nuclear data in table 11, primarily from [81]. The half-life for the decay of ^{196}Au^{g} is from [27]; a slightly longer half-life (6.183 d) [81] is in common use in radiochemistry, but in examining its pedigree it was not convincing that the precursor decay of ^{196}Au^{m2} was treated correctly in the reported measurements. The nuclear data for ^{197}Pt^{g} comes from a recent evaluation [130].

The data are used in absolute atom calculations similar to the method outlined for the representative calculation of table 1. In table 12 the values obtained for the concentrations of the products of minor reactions relative to that of ^{196}Au^{g}, or their limits (one-sigma) are reported. All reported values are averages of the data collected from the three indicated

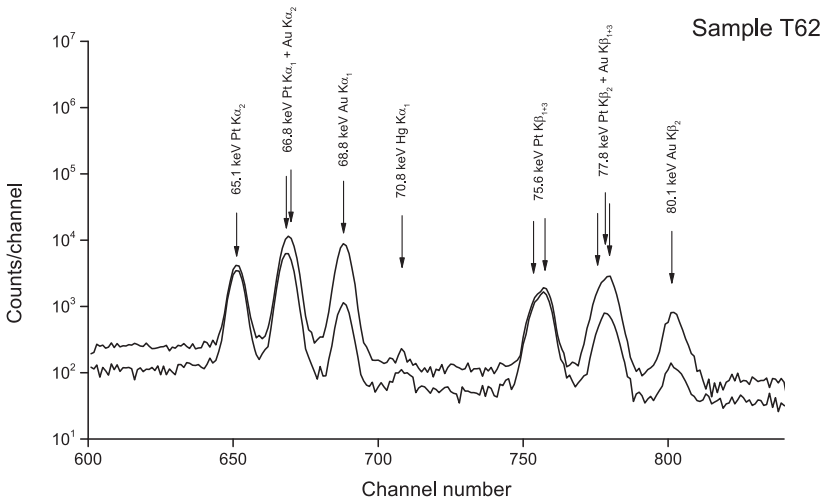

Figure 9. Two low-energy photon spectra obtained from sample T62, taken with a LEPS detector at approximate times of 2.7 and 45.8 h after irradiation, scaled to 2.5 h of acquisition time. The *x*-ray transitions contributing to each photopeak are shown in the spectrum. The decay of the gold *K* *x*-rays (associated with 9.6 h $^{196}Au^{m2}$ decay) relative to the platinum *K* *x*-rays (associated with 6.2 d $^{196}Au^{g}$ decay) is apparent when comparing the two spectra.

Table 12. Reaction product radionuclide atom ratios measured in NIF irradiations of gold foils. The data are weighted averages over several samples as described in the text.

Nuclides	Atom ratio
$^{196}Au^{m2}/^{196}Au^{g}$	0.0731 ± 0.0019
$^{195}Au/^{196}Au^{g}$	$\leqslant 4.0 \times 10^{-3}$
$^{197}Pt^{m}/^{196}Au^{g}$	$4.9(1.1) \times 10^{-4}$
$^{197}Pt^{g}/^{196}Au^{g}$	$\leqslant 3.8 \times 10^{-3}$
$^{194}Ir/^{196}Au^{g}$	$\leqslant 6 \times 10^{-4}$
$^{198}Au^{m}/^{196}Au^{g}$	$\leqslant 7.5 \times 10^{-5}$
$^{198}Au^{g}/^{196}Au^{g}$	0.10 ± 0.02

samples, except those given for $^{196}Au^{m2}/^{196}Au^{g}$ (table 9) and for $^{198}Au^{g}/^{196}Au^{g}$ (from all samples). The propagated statistical uncertainty associated with the $^{198}Au^{g}/^{196}Au^{g}$ value is much smaller than given in table 12, but does not capture the spread in the atom ratio values from sample to sample. The $^{198}Au^{g}$ activity is produced by the $^{197}Au(n, \gamma)$ reaction, which has no energy threshold, so neutrons from the non-reproducible NIF room return interactions have an inordinately large effect on the source inventories of $^{198}Au^{g}$ (see section 5.4).

4.6. Decay curve analyses of the K x-ray photopeaks in spectra from samples T62 and T65

The *x*-rays accompanying the decays of the gold isotopes can give information regarding the internal conversion of electromagnetic transitions, particularly for decays that are not accompanied by a change in atomic number, such as $^{196}Au^{m2}$. In figure 9 sections of two photon spectra are shown that were taken with a LEPS detector from the thin gold sample T62. One spectrum was acquired shortly after the NIF irradiation while the other was taken

after an elapsed time of more than four $^{196}Au^{m2}$ half-lives. Transitions contributing to each photopeak are designated in the figure.

The decays of the gold isotopes produce *x*-rays in their daughter nuclei, so characteristic *K x*-rays from platinum, gold, and mercury are potential contributors to the observed intensities. For those elements, the *K x*-rays from radioactive decay overlap [131], with the $K\alpha_1$ peak from element *Z* overlapping the $K\alpha_2$ peak from element $(Z + 1)$, and the $K\beta_2$ peak from element *Z* overlapping the $K\beta_{1+3}$ peak from element $(Z + 1)$. As a result, many of the *K x*-ray photopeaks in the experimental spectra are multiplets unresolved by GAMANAL, each of them a potential contributor to be assayed through decay curve analysis. From table 12 it is known that only $^{196}Au^{m2}$, $^{196}Au^{g}$, and $^{198}Au^{g}$ are likely to contribute significantly to the *K x*-ray intensity emitted by the sources. The EC decay of $^{196}Au^{g}$ is the only contributor to the platinum *K x*-rays. The β^- decays of $^{196}Au^{g}$ and $^{198}Au^{g}$ can contribute mercury *K x*-rays. The β^- decay process itself does not produce many *K*-shell vacancies, and the accompanying γ-rays (426 and 411 keV) are of *E*2 multipolarity and of relatively high energy such that the transitions are not significantly converted [132, 133]. This is confirmed by the observed intensity of the Mercury $K\alpha_1$ line in figure 9, so it is assumed that the contribution of the β^- decaying radionuclides to the intensities of the major *K x*-ray peaks is negligible.

The nuclear-decay component of the gold *K x*-ray intensity comes from internal conversion of the γ transitions in the IT decay of $^{196}Au^{m2}$. From table 12, the only other potential contribution to the production of gold *K x*-rays in nuclear decay is $^{198}Au^{m}$, which is produced at sufficiently low levels as to be unobservable in these experiments. By comparing the two spectra shown in figure 9, gold *K x*-ray contributions to the photopeaks decay more rapidly than the contributions from platinum *K x*-rays as expected. Based on the time elapsed between the acquisition of the two spectra, it is expected that *K x*-ray intensity due to decays of $^{196}Au^{m2}$ will have decreased by more than a factor of 20, but even those photopeaks that have no admixture of platinum *K x*-ray intensity (e.g. 68.8 keV) have not decayed by that much. Excess long-lived gold *K x*-ray intensity results from the contribution of fluorescence of the gold sample matrix induced by the gross radioactivity of the sample; i.e. from *K* vacancies excited by photoelectric absorption and Compton scattering of photons [90, 134, 135]. The nuclear-decay component of the observed gold *K x*-ray intensity is proportional to the decay rate of $^{196}Au^{m2}$ in the sample. The fluorescence component is proportional to some combination of the decay rates of all the gold isotopes and to the mass of activated gold in the source. Fluorescence processes do not contribute to the observed intensities of the platinum or mercury *x*-rays, however, because the sample matrix has negligible mass admixtures of those elements.

In order to determine the *K x*-ray intensity associated with the nuclear decay of $^{196}Au^{m2}$, two-component decay-curve analyses were performed on the six major *K x*-ray photopeaks emitted by two sources that contained significantly different amounts of gold, sample T62 (0.93 g) and sample T65 (2.50 g). The two components were assumed to decay with the half-lives of $^{196}Au^{m2}$ and $^{196}Au^{g}$, which were held constant in the calculations. This treatment should be considered semiquantitative; the decay of sample T65 was followed with a COAX detector with an efficiency calibration that was not perfectly modeled for photons with energy $<$70 keV. The attenuation of photons with energies below the gold *K* edge (80.7 keV [97]) is substantial, particularly for sample T65 where attenuation by an interposed cadmium foil and self-attenuation by the thick gold sample are shown in figure 7. In the decay-curve analyses, it was assumed that no significant contribution to the fluorescence of the sample was due to decays of $^{198}Au^{g}$, and no ingrowth of $^{196}Au^{g}$ was from the decays of $^{196}Au^{m2}$, an approximation supported by the data shown in figure 8.

Table 13. Two-component decay-curve analyses of the six principal *x*-ray photopeaks determined in the decays of the indicated gold samples. Component half-lives were held fixed in the calculations. Data units are absolute photons/min. Uncertainties are one-sigma.

Sample	Photon energy (keV)	Contributing x-ray transitions	Initial contribution 9.6 h activity	Initial contribution 6.17 d activity
T62	65.1	Pt $K\alpha_2$	-389 ± 106	10946 ± 19
(thin)	66.8	Pt $K\alpha_1$ + Au $K\alpha_2$	13095 ± 186	19840 ± 23
	68.8	Au $K\alpha_1$	25103 ± 101	1983 ± 8
	75.6	Pt $K\beta_{1+3}$	-332 ± 138	6378 ± 31
	77.8	Pt $K\beta_2$ + Au $K\beta_{1+3}$	8574 ± 126	2401 ± 12
	80.2	Au $K\beta_2$	3571 ± 66	344.1 ± 7.1
T65	65.1	Pt $K\alpha_2$	196 ± 1686	28798 ± 407
(thick)	66.8	Pt $K\alpha_1$ + Au $K\alpha_2$	43760 ± 3350	52420 ± 660
	68.8	Au $K\alpha_1$	77020 ± 1840	9553 ± 149
	75.6	Pt $K\beta_{1+3}$	-228 ± 575	15370 ± 140
	77.8	Pt $K\beta_2$ + Au $K\beta_{1+3}$	22570 ± 610	7489 ± 75
	80.2	Au $K\beta_2$	17820 ± 540	2051 ± 68

Table 14. Literature values of *x*-ray intensities per *K* vacancy for relevant elements [136, 137], and the *K*-shell fluorescence yields [60]. Photons arising in $K\beta_1$ and $K\beta_3$ transitions were not resolved in the analyses presented here, so the intensity information is given for the sum, $K\beta_{1+3}$.

	Intensity per *K* vacancy		
x-ray photon	Pt	Au	Hg
$K\alpha_2$	0.274 ± 0.006	0.275 ± 0.006	0.275 ± 0.006
$K\alpha_1$	0.465 ± 0.010	0.464 ± 0.010	0.463 ± 0.009
$K\beta_{1+3}$	0.1626 ± 0.0025	0.1627 ± 0.0025	0.1629 ± 0.0025
$K\beta_2$	0.0381 ± 0.0008	0.0384 ± 0.0008	0.0387 ± 0.0008
Fluorescence yield	0.963	0.964	0.966

The results of the two-component decay-curve analyses of the six principle *K* *x*-ray photopeaks in samples T62 and T65 are given in table 13. For the 65.1 and 75.6 keV transitions, which include no contributions from gold *K* *x*-rays, a small negative activity for the 9.6 h decay component can arise, due in part to ingrowth of $^{196}Au^{g}$ from $^{196}Au^{m2}$ decay. The magnitude of the component is small relative to the positive contributions of the 9.6 h component to the other photopeaks, supporting the two-component decay-curve approximation. The relative intensities of the *K* *x*-ray photopeaks associated with each element are well known [136, 137] and are given in table 14 as photons emitted per *K* vacancy for the four principle *x*-ray photon groups ($K\alpha_2$, $K\alpha_1$, $K\beta_{1+3}$, and $K\beta_2$).

With the values from table 14, the data in table 13 can be converted to four values each of *K* vacancies/min at the end of irradiation for platinum *K* *x*-rays arising in $^{196}Au^{g}$ EC decay, gold *K* *x*-rays from the fluorescence of the sample medium from the decay of $^{196}Au^{g}$, and gold *K* *x*-rays arising from the sum of the IT decay of $^{196}Au^{m2}$ and the fluoresce of the medium by $^{196}Au^{m2}$. The four individual measurements of the initial *K* vacancy rate of each type were

Table 15. Calculation of the initial K vacancy rate of $^{196}Au^{m2}$ due to nuclear decay processes.

Sample ID	Mass (g)	Pt K vacancies 6.18 d half-life	Au K vacancies 6.18 d half-life	Au K vacancies 9.6 h half-life
T62	0.9292	39900 ± 520	3927 ± 66	52010 ± 690
T65	2.5021	98360 ± 1460	22270 ± 420	161900 ± 3300
T62		$\frac{\text{observed } ^{196}Au^{m2} \text{ Au } K \text{ vac.}}{\text{observed} ^{196}Au^{g} \text{ Pt } K \text{ vac.}} = 1.303 \pm 0.024$		
T65		$\frac{\text{observed } ^{196}Au^{m2} \text{ Au } K \text{ vac.}}{\text{observed } ^{196}Au^{g} \text{ Pt } K \text{ vac.}} = 1.646 \pm 0.042$		
		$\frac{9.6 \text{ h Au } K \text{ } x\text{-rays due to fluorescence}}{^{196}Au^{g} \text{ Pt } K \text{ vac.}} = 0.218 \pm 0.031 \text{ g}^{-1}$		
T62		$\frac{^{196}Au^{m2} \text{ internal conversion Au } K \text{ } x\text{-rays}}{188.2 \text{ keV photon intensity}} = 2.677 \pm 0.134$		

determined from photopeaks spanning the energy range of 65–80 keV. The results were consistent with computational uncertainties associated with the counting statistics of the spectra obtained from each sample, indicating the GAMANAL attenuation corrections were applied appropriately. The weighted averages of the initial K vacancy rates for both samples are listed in table 15.

1t is assumed that the isomer ratio $^{196}Au^{m2}/^{196}Au^{g}$ is the same in both samples, arising primarily from the reaction of 14.1 MeV neutrons with ^{197}Au. This is supported by the measurements presented in table 10. If fluorescence of the medium was unimportant, the initial rate of gold K x-ray vacancies decaying with a 9.6 h half-life, divided by the initial rate of platinum K vacancies decaying with a 6.2 d half-life, would be constant. As shown in table 15, this is not the case. These data can be used to extract the 9.6 h K vacancy rate due to fluorescence processes as a function of the mass of gold in the sample. This correction factor was applied to the thin-foil T62 data to arrive at the rate due to nuclear decay processes, and the T62 data in tables 10 and 14 were used to normalize this value to the intensity of the 188.2 keV photon. There are (2.677 ± 0.134 (±5%)) internal-conversion K vacancies for each 188.2 kev photon emitted in the IT decay of $^{196}Au^{m2}$.

5. Discussion

In section 4, the γ-ray spectrometric measurements of the decay properties of $^{196}Au^{m2}$ and other products of the reaction of fast neutrons with ^{197}Au were presented. In this section, application of these results to the NIF diagnostic measurements is made. Isomerism and the nuclear structure of ^{196}Au will be discussed, as well as a method for calculating reaction cross sections for the production of radionuclides by the complicated neutron spectrum generated through the fusion of the DT fuel in a NIF capsule.

5.1. A fidelity check of the present $^{196}Au^{m2}$ decay data

In section 1, a calculation of the $^{196}Au^{m2}$ content of a representative sample of NIF debris was presented as motivation for remeasuring its nuclear-decay properties. Table 16 reproduces the calculation in table 1, but replaces the literature data with those obtained in this work from irradiated gold foils. The standard deviation of the three values of the relative disintegration rate derived from the three strongest γ-lines is now 1.3%, compared with 21% obtained in table 1 using the literature data. This is comparable to the propagated uncertainty of 1.0%.

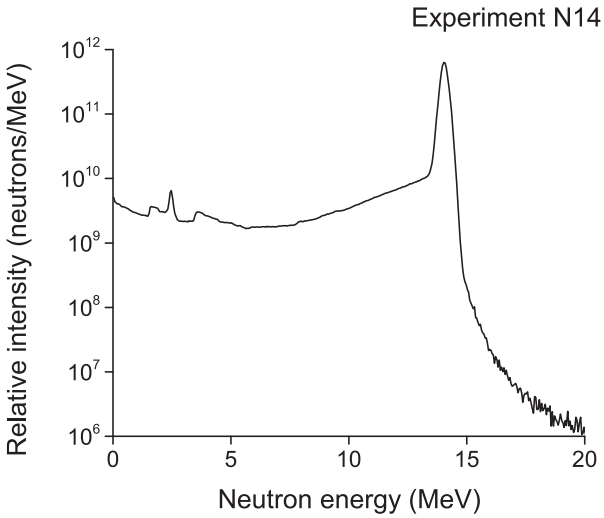

Figure 10. A simulation of the energy spectrum of neutrons emitted from the fusion capsule deployed in NIF experiment N141106.

Table 16. Calculation of the $^{196}Au^{m2}$ content of debris sample CC6870, experiment N150416, first count after sample recovery, applying the nuclear decay data measured in this work. Direct comparison to table 1 is instructive.

Photon energy (keV)	Measured photons/min	Spectroscopic relative intensity	Relative disintegrations/min
147.8	8199 ± 141	1.2614 ± 0.0128	6500 ± 130
168.4	1100 ± 33	0.1736 ± 0.0018	6336 ± 201
188.3	6461 ± 85	1.00	6461 ± 85
		Weighted average	6457 ± 67
		Normalization	0.3352 ± 0.0097
		Decay rate	19260 ± 590

Even though the resulting decay rate (19260 ± 590) is not significantly different from that obtained with the literature data (18690 ± 1430), the improvement in data quality is obvious.

5.2. The calculation of cross sections relative to a reference value for NIF neutrons

Members of the nuclear science community have been interested in using the neutron pulse emitted by a NIF fusion capsule for the measurement of nuclear reaction cross sections [6]. Unfortunately, as discussed in section 1, scattering processes in the compressed thermonuclear fuel affect the NIF neutron spectrum such that it is not monoenergetic. This is a valuable characteristic for diagnosis of capsule performance, but less desirable for fundamental physics measurements of reaction cross sections.

Figure 10 shows the spectrum of neutrons produced by the capsule fuel in experiment N141106 (see table 2). The spectrum is the result of a computational simulation [10, 138], supported by the prompt-diagnostic measurements of the neutron spectrum for that experiment [12–14, 139, 140]. The spectra calculated for the other experiments in table 2 are similar in general form. The contribution of more thermalized room-return neutrons at the irradiation

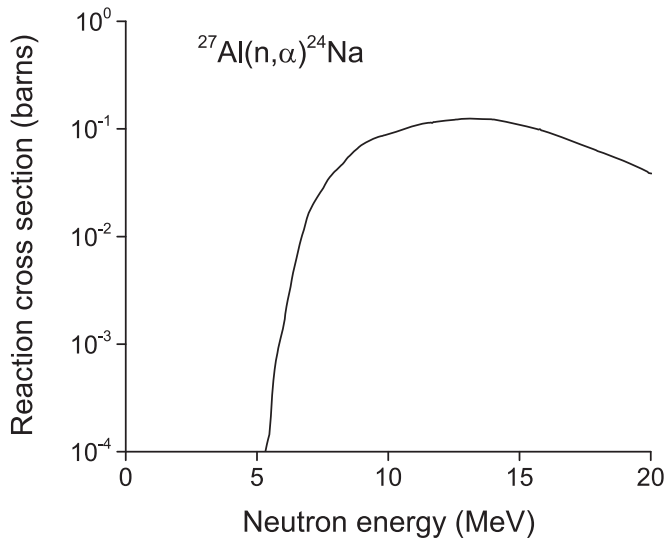

Figure 11. Excitation function for the ^{27}Al(n, α)^{24}Na reaction [16, 144].

location is not included, but it is projected to be an important contribution only at sub-MeV energies [9]. The spectrum is dominated by the primary neutrons, with energies between 13 and 15 MeV. The secondary neutrons contributing to the spectrum below 13 MeV are the result of one or more scattering interactions, mostly in the compressed thermonuclear fuel [10, 11, 141]. The neutrons at energies >15 MeV arise from reactions-in-flight [142, 143], in which deuterons or tritons elastically scattered to higher energies by primary neutrons subsequently undergo fusion reactions.

The flux monitor reaction used in these measurements is ^{27}Al(n, α)^{24}Na, with an excitation function shown in figure 11 [16, 144]. The peak cross section is between 13 and 15 MeV, where it is only weakly dependent on neutron energy. The total production of ^{24}Na is proportional to the integral-over-energy of the product of the neutron spectrum (figure 10) and the excitation function (figure 11). That calculation indicated that 92.5% of the ^{24}Na produced in experiment N141106 can be attributed to reactions of ^{27}Al with neutrons of energies between 13 and 15 MeV, the activation fraction due to primary neutrons. The areal density of the target, the reaction cross section at 14.1 MeV (0.121 b [144]), and the empirical production of ^{24}Na, combine for a determination of the number of primary neutrons that passed through the aluminum target. Scaling this value by the relative target areas, the derived flux can be applied to the calculation of cross sections for primary neutron reactions in the associated gold foil. The uncertainty of the ^{27}Al(n, α) cross section at 14 MeV is approximately 1.5% [145, 146] or less [147].

The ^{197}Au(n, 2n) excitation function is well known [16, 148]; however, the method of calculating the cross section for reactions with primary neutrons without including this information must be developed. The form of the excitation functions for (n, 2n) reactions on odd–even nuclides in the (Z, N) vicinity of ^{197}Au (Z = 75–83) is only slowly varying, rising from a cross section of zero at the energy threshold of the reaction to a plateau between 13 and 15 MeV. A hypothetical, non-normalized excitation function for ^{197}Au(n, 2n) was created based on the reaction threshold at 8.03 MeV [84] and the energy dependence relative to thresholds of (n, 2n) reactions of nearby odd–even targets [16], compared as semilogarithmic plots. Folding the derived excitation function with the neutron spectrum in figure 10, the

Table 17. Cross section for the reaction ^{197}Au(n, $2n$)^{196}Au^{g} with primary neutrons from γ-ray spectrometry of the indicated samples. The irradiations are described in table 2. Source areas and masses of the gold foils are given in table 3.

Sample ID	Al monitor (per 5.02 cm^2)	^{24}Na production (atoms)	^{196}Au^{g} production (atoms)	^{197}Au(n, $2n$)^{196}Au^{g} cross section (b)
T65	32.6 mg	8.550(68) × 10^6	1.424(16) × 10^9	1.959 ± 0.027
T63	32.7 mg	9.590(134) × 10^6	6.234(69) × 10^8	2.040 ± 0.036
T64	32.5 mg	1.000(12) × 10^7	6.251(69) × 10^8	1.958 ± 0.032
			Weighted average	1.979 ± 0.026

resultant estimate was that 94.5% of the production of ^{196}Au comes from reactions with neutrons between 13 and 15 MeV. This is sufficiently close to 100% that there is justification for assigning an uncertainty of 1% to this activation fraction.

The simulation shown in figure 10 does not have an associated uncertainty, so its contribution to calculation of the uncertainties of the individual activation fractions is not known. However, the shape of the neutron spectrum affects the inventory of both reaction products (^{24}Na and ^{196}Au) in similar fashion, making unquantified uncertainties in the calculated spectrum partially cancel when computing the ratio of activation fractions used for the determination of cross sections. Although similar in general form, the simulated spectra for the other experiments listed in table 2 may be different in detail. From table 2, it is noted that yields of the capsules fielded in experiments N141106 and N151020 were similar, implying a similar degree of fuel compression and, consequently, a similar degree of downscatter; this was verified by prompt-diagnostic measurements, which indicated that the ratio of the intensity of downscattered neutrons to that of primary neutrons was similar in both experiments. Spectrometric data were selected from samples irradiated in these two experiments (T65, T63, and T64) as the basis of the ensuing cross-section calculations.

The calculations of the cross sections for ^{197}Au(n, $2n$)^{196}Au^{g} from primary neutrons are outlined in table 17, based on the flux extracted from the ^{27}Al(n, α)^{24}Na monitor reaction and data from γ-ray spectrometry of the three indicated samples. In these analyses, ^{196}Au^{g} and ^{196}Au^{m2} were calculated independently. The isomer ratio is small (~0.07) and it was assumed to vary insufficiently between 13 and 15 MeV such that the cross section for the production of ^{196}Au^{g} remained constant across the energy window (see section 5.3). The cross section for ^{197}Au(n, $2n$)^{196}Au^{g} was derived and converted to ^{197}Au(n, $2n$)^{196}Au through application of the isomer ratio.

The three calculations outlined in table 17 give similar results for the ^{197}Au(n, $2n$)^{196}Au^{g} cross section. The weighted average of the three measurements is 1.979 b ± 0.026 (±1.3%). The total cross section for the production of the sum of all isomeric states (^{196}Au^{t}) is obtained by multiplying by (1 + I), where I is the isomer ratio reported in section 5.3. Propagating the uncertainty with those associated with the two activation fractions and the isomer ratio, a reaction cross section for ^{197}Au(n, $2n$)^{196}Au^{t} of 2.124 b ± 0.055 (±2.6%) is obtained. The error bar should be considered a minimum since it does not include uncertainties inherent in the simulation of the neutron spectrum, which have not yet been evaluated.

The as-reported literature cross sections for the ^{197}Au(n, $2n$)^{196}Au^{t} reaction are presented in table 18 along with the cross section derived from this work for comparison. Data from references published prior to 1965 are excluded. Included are cross section values for reactions induced by neutrons with energies in the vicinity of 14.1 MeV.

Table 18. As-reported ^{197}Au(n, $2n$) cross sections near 14 MeV. Data are from the listed references, excluding work reported prior to 1965. The derived cross section from this work is included for comparison. The error bar on the present measurement is a minimum value that does not contain systematic uncertainties discussed in the text.

E_n (MeV)	Cross section (mb)	References
14.8	1950 ± 20	[76]
14.7	2150 ± 100	[149]
14.72	2149 ± 100	[150]
14.7	2209 ± 253	[151]
14.4	1986 ± 150	[29]
14.10	2213 ± 94	[152]
14.89	2116 ± 89	[152]
14.05	1850 ± 100	[153]
14.60	1880 ± 105	[153]
14.7	2064 ± 125	[154]
13.8	2039 ± 91	[155]
14.28	1936 ± 97	[155]
14.76	1935 ± 155	[155]
14.68	2170 ± 67	[31]
14.75	2071 ± 93	[156]
14.50	2151 ± 43	[157]
14.10	2211 ± 88	[147]
14.45	2153 ± 86	[147]
14.65	2105 ± 84	[147]
14.80	2158 ± 86	[147]
14.1 (13–15)	2124 ± 55	This work

The result for the ^{197}Au(n, $2n$) cross section obtained in this work is comparable with data presented in the modern literature. The method developed to calculate the fraction of the activation product inventory due to interactions of primary neutrons, in reactions with energy thresholds above the contribution of room-return neutrons, appears successful. However, the calculation is based on a simulated neutron spectrum, the fidelity of which is a key issue in the application of the method. At this time, there is insufficient information to propagate any uncertainties associated with the simulation into an overall uncertainty in the activation fraction.

5.3. The $^{196}Au^{m2}/^{196}Au^{m1+g}$ isomer ratio

As described in the previous section, the calculation of a primary-neutron induced cross section via the comparison of similar reactions depends on the excitation functions for both reactions being roughly constant between 13 and 15 MeV. Systematics indicate that this is true for ^{197}Au(n, $2n$)^{196}Au^t, but would be true for ^{197}Au(n, $2n$)^{196}Au^g only if the change in the ^{196}Au$^{m2}/^{196}$Au^g isomer ratio across the primary neutron energy window has minimal effect on ^{196}Au$^g/^{196}$Au^t.

Since nuclear isomers have the same mass number, physical techniques involving reaction kinematics or isotope separation are inappropriate for the accurate determination of an isomer ratio; counting techniques for measuring characteristic radioactive emissions are required in most cases. As a result, there are fewer determinations of the ^{196}Au$^{m2}/^{196}$Au^{m1+g} isomer ratio from the ^{197}Au(n, $2n$) reaction than there are cross section measurements for the

Table 19. ^{196}Au isomer ratio ($^{196}Au^{m2}/^{196}Au^{m1+g}$) near 14 MeV measured via the ^{197}Au(n, $2n$) reaction.

E_n (MeV)	Isomer ratio	References
14.5	0.106 ± 0.030	[158]
14.5	0.063 ± 0.004	[159]
14.5	0.061 ± 0.005	[77]
14.8	0.134 ± 0.012	[76]
14.7	0.068 ± 0.009	[160]
14	0.079 ± 0.008	[38]
14.4	0.082 ± 0.012	[29]
14	0.08 ± 0.01	[30]
14.3	0.068 ± 0.003	[31]
14.10	0.0876 ± 0.0049	[147]
14.45	0.0940 ± 0.0052	[147]
14.65	0.0998 ± 0.0058	[147]
14.8	0.0938 ± 0.0052	[147]
14.1 (13–15)	0.0731 ± 0.0019	This work

production of $^{196}Au^{t}$ (table 18). Literature values for the isomer ratio at relevant reaction energies are summarized in table 19, along with the value determined in this work. Since the present determination is derived from the radioactive ingrowth measured in individual γ-lines, it is independent of γ-ray intensity data for the nuclear decay of $^{196}Au^{m2}$ available prior to this measurement. Consequently, it can be argued that the value obtained here is more accurate, even though the reaction energy is less constrained.

The data presented in table 19 indicate enough bias in the literature that comparison of individual measurements is unlikely to identify an energy dependence of the isomer ratio. Evaluated excitation functions for ^{197}Au(n, $2n$)$^{196}Au^{m1+g}$ and ^{197}Au(n, $2n$)$^{196}Au^{m2}$ exist [16], but the $^{196}Au^{m2}$ evaluation is most strongly influenced by the oldest experimental data, poorly reproducing most of the more recent data, and yielding a much higher isomer ratio than measured in these experiments. Nevertheless, the isomer ratio as a function of incident neutron energy shows an increase of approximately 25% between 13 and 15 MeV.

Examination of the cross sections for the products of neutron induced reactions well beyond their threshold energies shows that most isomer ratios are only moderately sensitive to the incident neutron energy [161, 162]. For reactions near threshold, however, this is clearly not true; for instance, for incident neutron energies between 8.03 and 8.63 MeV, only the ^{196}Au ground state is energetically accessible, and the $^{196}Au^{m2}/^{196}Au^{g}$ isomer ratio is identically zero [84, 85]. At the other extreme, in the case of the reaction of primary fusion neutrons with ^{197}Au, the spin of the isomer is unusually high, beyond the majority of the distribution of angular momentum produced in the compound nucleus (see below), leading to a low isomer ratio that may be unusually sensitive to changes in projectile energy [163].

In reactions between heavy nuclei and neutrons with energies up to 15 MeV, radionuclide production is dominated by processes subsequent to the formation of a compound nucleus [164] where the excitation energy and orbital angular momentum imparted by the Collison are acquired by the nucleus as a whole [165]. For a reasonably quantitative calculation of radionuclide inventory, it is unnecessary to consider more direct (e.g. precompound) reactions until neutron energies exceed 20 MeV [152, 163, 166, 167], and there are very few such neutrons produced in a NIF capsule (figure 10).

In the classical approximation of colliding hard spheres, if a central (on-axis) collision and absorption between a neutron and ^{197}Au is considered, the angular momentum imparted to the compound nucleus is some combination of the spin of the neutron ($J = 1/2$) and the spin of the gold nucleus ($J = 3/2$) [81], independent of projectile energy, because there is no relative orbital angular momentum. Given the radius of the nucleus [168], incoming neutrons at the (n, $2n$) threshold energy (8.1 MeV) impart no more than six units of orbital angular momentum to the compound nucleus. For incident neutrons at 15 MeV, the hard-sphere compound nucleus acquires no more than nine units of angular momentum. Therefore, while the compound nucleus acquires an additional 7 MeV of excitation energy between the (n, $2n$) threshold and 15 MeV, the average value of the distribution of angular momentum changes by some fraction of three units, peaking at spins below that of the metastable state.

The simple model involving hard spheres does not impart enough angular momentum to the ^{198}Au compound nucleus to produce significant amounts of $J = 12$ ^{196}Au^{m2}. The distribution of angular momentum of the compound nucleus was calculated using the Hauser-Feshbach formalism based on penetrabilities and the optical model [168–171]. In this model, fast neutrons approach the target nucleus following a trajectory characterized by a classical impact parameter that corresponds to an orbital angular momentum of $\ell \times h/2\pi$, where ℓ is the orbital-angular-momentum quantum number. The reaction coordinate defines the z-axis of the system for quantum-mechanical projections of the angular momentum. Each partial wave combines with the intrinsic spins of the neutron and the ^{197}Au target nucleus to distribute the cross section associated with ℓ, proportional to $(2\ell + 1)$, and the square of the wavelength of the incoming neutron. The distribution is among states in the compound nucleaus from $\ell - 2$ to $\ell + 2$, weighted according to the squares of the Clebsch–Gordon coefficients describing the coupling of the three angular momentum vectors [169, 172, 173].

Since the NIF neutron spectrum is not strictly monoenergetic (figure 10), the angular momentum distributions for compound nuclei arising in the reactions of 13.1, 14.1, and 15.1 MeV neutrons with gold were calculated. These calculations are shown in figure 12. The ^{198}Au compound nucleus excitation energy induced by 14.1 MeV incident neutrons is 20.5 MeV [84]. Deexcitation of high-Z compound nuclei is assumed to be dominated by neutron emission from excited states with energies significantly above the yrast line, and by photon emission for excited states less than one neutron binding energy above the yrast line [162, 174, 175]. The yrast line [176], the minimum excitation energy at each value of the angular momentum due to nuclear spin, can be calculated from the rotating liquid-drop (RLD) model [177, 178]. The yrast line for ^{196}Au is shown in figure 13, overlaid with experimental values of the lowest energy levels at each nuclear spin reported in the literature [27], demonstrating that the RLD calculation is reasonable. States with excitation energies within 6.6 MeV [84] of the yrast line have insufficient energy to emit another neutron. The nuclear rotation energy does not exceed 1 MeV until $J > 14$.

Emission of a neutron from the ^{198}Au compound nucleus at 20.5 MeV results in states in ^{197}Au with no more excitation energy than 14.0 MeV. Emission of a second neutron populates states in ^{196}Au with no more excitation energy than 6.0 MeV, below the energy necessary to emit yet another neutron to form ^{195}Au (see section 5.4). The emission of neutrons can affect the angular momentum of the residual nucleus and small changes in residual angular momentum are favored over larger ones [178], influenced by the level density of receiving states. The level density of states at high excitation energies is given by Lang [179],

$$\rho(E, J) \propto (2J + 1)E^{-2} \exp(\{2\alpha[E - B(J)]\}^{1/2}), \tag{7}$$

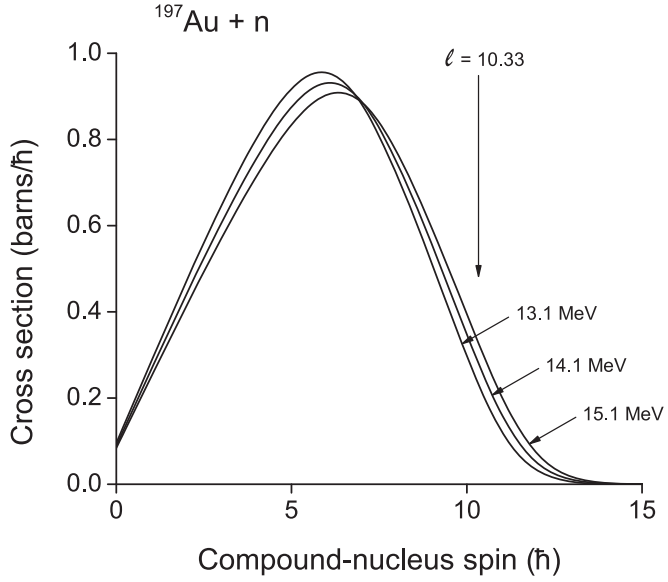

Figure 12. The distribution of angular momentum in the ^{198}Au compound nucleus formed in the reaction of ^{197}Au with incident nuetrons of energies 13.1, 14.1, and 15.1 MeV. For the 14.1 MeV curve, the ratio of the integral cross sections above and below the vertical arrow at $\ell = 10.33$ MeV equals the isomer ratio observed in the reported experiments.

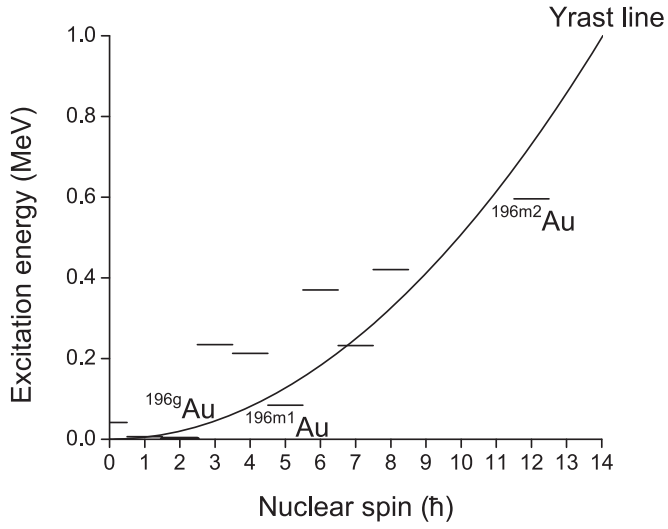

Figure 13. The yrast line for ^{196}Au, with the lowest-energy states at each angular momentum shown for comparison. The three isomeric states are labeled.

where E is the excitation energy, J is the nuclear angular momentum, α is the level-density parameter ($\alpha \cong 20$ for ^{198}Au [178]) and $B(J)$ is the energy of the yrast line at spin J [179].

In the gold isotopes under discussion, the $(2J + 1)$ factor balances the exponential term in equation (7) such that at a given excitation energy above 5 MeV, the level density is

relatively constant for angular momenta between $\ell = 6$ and $\ell = 13$. As a result, the angular momentum distribution shown in figure 12 for ^{198}Au at 20.5 MeV can be thought of as a 'settling' toward the yrast line, resulting in similar spin distribution in the states in ^{196}Au below 6 MeV, which deexcite through the sequential emission of photons to result in the radiochemical observables. Since emission of dipole photons dominates over emission of photons of higher multipolarity [180–182], sequential photon emission from continuum states above $J = 12$ results preferentially in the eventual population of the second metastable state, while those in the vicinity of $J = 12$ populate both metastable states (figure 13). In figure 12 a vertical arrow is shown at $\ell = 10.33$, an experimentally justified spin cut-off parameter [174]. For the reaction of ^{197}Au with 14.1 MeV neutrons, the ratio of the integral cross section above $\ell = 10.33$ to that below $\ell = 10.33$ reproduces the experimental isomer ratio, $I = 0.073$.

Applying the same spin cut-off parameter to the angular momenta arising in 13.1 MeV and 15.1 MeV irradiations results in isomer ratios of 0.057 and 0.091, respectively, an increase of 46% across the primary neutron energy window. This is actually an overestimate of the energy dependence of the isomer ratio. As the excitation energy of the ^{196}Au residual nucleus increases, the paths by which states above $J = 12$ can bypass the ^{196}Au^{m2} yrast trap [183] (see figure 13) and pass decay intensity to states of lower multipolarity also increases, resulting in an increase in the spin cut-off parameter and a reduction in the isomer ratio. The absolute magnitude of the isomer ratio is small, and the neutron energy spectrum is strongly peaked at 14.1 MeV. Thus, even if the isomer ratio changes significantly across the primary neutron energy window, the primary neutron production of ^{196}Au^{g} is always >90% that of ^{196}Au^{t}, validating the calculation of the ^{197}Au(n, $2n$)^{196}Au^{g} cross section via comparison.

The measured isomer ratio reported in table 19 is integral, containing a contribution from the portions of the neutron energy spectrum outside the primary neutron energy window. As a worst-case scenario, the isomer ratio for reactions between threshold and 13 MeV is assumed to be identically zero. Given the activation fraction of 94.5% determined in section 5.2, the isomer ratio induced by primary neutrons alone could increase by as much as 5.5% from $I = 0.073$ to $I = 0.077$. Since the conversion of ^{197}Au(n, $2n$)^{196}Au^{g} calculated in table 17 to the cross section for ^{197}Au(n, $2n$)^{196}Au^{t} reported in table 18 comes about by multiplying by $(1 + I)$, the most drastic adjustment to the isomer ratio results in a change in the cross section for the production of ^{196}Au^{t} of 0.4%, much less than the uncertainty on the determination.

Given a neutron spectrum such as that shown in figure 10, small changes in capsule performance are not likely to produce an observable shift in the isomer ratio from the contribution of secondary neutrons. However, if future capsule designs achieve an improved fuel compression, these measurements may be of sufficient accuracy to develop ^{196}Au$^{m2}/^{196}$Au^{g} as a performance diagnostic. Evolution of the traditional nuclear production of ^{196}Au$^{m2}/^{196}$Au^{g} in the capsule must be understood before the study of the predicted effects of the fusion plasma on reaction rates can be undertaken [32, 33].

5.4. The production of other radionuclides

The neutrons from fusion reactions in a NIF capsule can induce radionuclides in gold other than the ^{197}Au(n, $2n$) products. The concentrations of these products relative to that of ^{196}Au^{g} are quantified in table 12. The isomer ratio ^{196}Au$^{m2}/^{196}$Au^{g} was discussed in section 5.3.

The cross section method outlined in section 5.2 does not apply to most of the isotope ratios presented in table 12. For example, the threshold energy of the ^{197}Au(n, $3n$) reaction, resulting in ^{195}Au, is 14.7 MeV [84]; since primary fusion neutrons do not produce ^{195}Au, the ratio of activation fractions is zero. The ^{197}Au(n, $3n$) excitation function rises from zero at 14.7 MeV and first exceeds 200 mb (10% of the maximum cross section) at an incident

neutron energy of 16.5 MeV [16]. Examination of the neutron spectrum in figure 10 and the production cross section for $^{196}Au^{g}$ in table 17 indicates that the atom ratio $^{195}Au/^{196}Au^{g}$ in these samples would not be expected to significantly exceed 10^{-5}, much lower than the limit actually measured. The long half-life of ^{195}Au and the low intensity of the γ-rays emitted in its decay (table 11) make the detection and interpretation of its production problematic. When higher fusion yields are attained at NIF, the ^{195}Au production rate may constitute a performance metric for reactions-in-flight [142, 143].

The irradiation of ^{197}Au with fast neutrons can also produce radionuclides by (n, p) and (n, α) reactions. Neither reaction has an energy threshold [84], but the incident neutron must supply sufficient energy that the evaporation of charged particles can overcome the internal Coulomb barrier of the compound nucleus. This results in a 'soft' onset of the two excitation functions at neutron energies in excess of 5 MeV [16], and cross sections that are far from constant for neutron energies between 13 and 15 MeV, thereby compromising the calculation of activation fractions. Nevertheless, the evaluated cross section for the $^{197}Au(n, p)$ reaction at 14.1 MeV is 2 mb, and that for the $^{197}Au(n, \alpha)$ reaction is 0.25 mb [148], resulting in $^{197}Pt/^{196}Au^{g} = 1.0 \times 10^{-3}$ and $^{194}Ir/^{196}Au^{g} = 1.2 \times 10^{-4}$. The measurements of atom ratio limits for $^{197}Pt^{g}/^{196}Au^{g}$ and $^{194}Ir/^{196}Au^{g}$, presented in table 12, are not sufficiently sensitive to infer a cross section limit that challenges the literature data; however, the measured limits are sufficiently close to expectations from the literature that one could propose that the radiochemical isolation of Pt and Ir from the overwhelming radioactivity of the decays of the gold isotopes [26] would result in radionuclide sources of ^{194}Ir and $^{197}Pt^{g}$ with readily observable decay rates.

The radioactive decay of 95 min $^{197}Pt^{m}$ was observed in specimens that were available within 2 h of the irradiation time. From table 12, a cross section for $^{197}Au(n, p)^{197}Pt^{m}$ at 14.1 MeV of 1.0 mb $\pm$ 25% is inferred. Previous measurements of the $^{197}Au(n, p)^{197}Pt^{t}$ cross section involved either recoil proton observation [184] or the radiochemical separation of 18.3 h $^{197}Pt^{g}$ [159, 185], which includes 97% of the precursor decay of shorter-lived $^{197}Pt^{m}$ [186]. The J^{π} values for $^{197}Pt^{g}$ and $^{197}Pt^{m}$ are $1/2^{-}$ and $13/2^{+}$, respectively [81]. Given the distribution of angular momentum in the compound nucleus shown in figure 12, the (n, p) reaction channel can be estimated to be split about evenly between the ^{197}Pt isomers, making the measurement consistent with the 2 mb cross section reported in the literature [16]. Based on the literature available at the time, this is the first report of the measurement of a previously unknown reaction cross section using neutrons from a NIF fusion capsule.

The cross section for $^{197}Au(n, \gamma)$ at 14 MeV is on the order of 1 mb [31, 187–189], resulting in a value of $^{198}Au/^{196}Au^{g}$ of 5×10^{-4}, far less than the value reported in table 12. From experiments in which radionuclides induced in the gold matrix of the hohlraum were measured, it is known that lower energy neutrons produced by scattering interactions in the compressed thermonuclear fuel can significantly increase the production of ^{198}Au [9]. Folding the neutron spectrum in figure 10 for experiment N141106 with evaluated cross sections [148] for the $^{197}Au(n, \gamma)$ reaction, an additional contribution to $^{198}Au/^{196}Au^{g}$ of 3×10^{-3} can be calculated, still far below the empirical value reported in table 12. Neutrons scattering off the NIF vacuum chamber and local structural elements bathe the TOADs with lower-energy, room-return neutrons. The increased distance from the source of primary neutrons and the magnitude of the excitation function at neutron energies below 1 MeV [148] dictates that the contribution of (n, γ) reactions from room return can no longer be ignored; in fact, it dominates. Approximately 96% of the inventory of ^{198}Au in the gold foils is due to reactions with room-return neutrons.

As discussed in section 2, the isomeric states in ^{198}Au have shell-model configurations similar to those in ^{196}Au, with a $J^{\pi} = 2^{-}$ ground state and a $J^{\pi} = 12^{-}$ metastable state. The

deexcitation of the compound nucleus described in section 5.3 results in ^{198}Au solely through the emission of γ-rays, a lower probability process than deexcitation involving emission of neutrons. Even though the (n, γ) reaction does not have an energy threshold like the (n, $2n$) reaction, reactions with neutrons of energies <7 MeV are not expected to produce a compound nucleus with sufficient angular momentum to populate the high-spin isomer in ^{198}Au. The neutron spectrum shown in figure 10 is expected to result in a $^{198}Au^{m}/^{198}Au^{g}$ isomer ratio similar to that observed in $^{196}Au^{m2}/^{196}Au^{g}$, approximately 0.07. However, this value must be scaled downward to account for the contribution of room-return neutrons to the production of $^{198}Au^{g}$. Therefore, a value of $^{198}Au^{m}/^{196}Au^{g}$ is predicted in table 12 to be approximately $0.07 \times (5 \times 10^{-4} + 3.0 \times 10^{-3}) \times (1.0 - 0.96) = 1.0 \times 10^{-5}$. The non-observation of $^{198}Au^{m}$ in the γ-ray spectra or as a precursor component in the decay of $^{198}Au^{g}$ is not surprising although with higher capsule yields it may become possible to study the poorly known ^{197}Au(n, γ)$^{198}Au^{m}$ cross section.

5.5. The multipolarity of the 188.2 keV transition in ^{196}Au

The multipolarities of the γ-transitions arising in $^{196}Au^{m2}$ decay were assigned by Wapstra *et al* [41] based on coincident photon counting and conversion-electron spectrometry. Modern evaluations have not significantly changed the original assignments [27]. Given the J^{π} assignments of the metastable and ground states, the transition multipolarities define the spins and parities of the intermediate states, shown in figure 3.

In section 4.6, it was established that the number of K vacancies in the IT decay of $^{196}Au^{m2}$, normalized to the intensity of the 188.2 keV γ-ray, is 2.677 ± 5%. From figure 3, it is anticipated that the γ transitions that contribute most to the production of K vacancies [132, 133] are the 174.9 keV $M4$ transition, the 147.8 keV $E2$ transition, and the 188.2 keV transition. The 188.2 keV transition is of either $M1$ or $M1 + E2$ multipolarity, based on the relative intensities of L and K x-rays [175]. The measurement of the intensities of the K x-rays provides a means of estimating the relative amounts of $M1$ and $E2$ character in the 188.2 keV γ-transition. This is supplemental to the previous report of the $E2/M1$ multipole mixing ratio of $\delta = +0.12(2)$ measured via relative γ-anisotropies [65].

Table 20 lists the γ-transitions with energies above the gold K edge in the decay of $^{196}Au^{m2}$. Also given are the relative photon intensities and assigned multipolarities [27], the conversion coefficients for promoting K-shell electrons [132, 133], and the resulting K vacancy rate associated with each transition. The K conversion coefficients are associated with a computational uncertainty of 0.1%, but suffer from a systematic uncertainty on the order of 2% [190]. In cases where both $M1$ and $E2$ multipolarities are thought to contribute to the decay intensity, the conversion coefficients and K vacancy rates for both are given; the K vacancy rates for these transitions are somewhere between the extremes. The multipolarity of the 263.8 keV transition is discussed in section 5.6.

Examination of table 20 shows that the 188.2 keV transition is the only one assigned with a mixed multipolarity that contributes significantly to the total K vacancy rate. If the weak 263.8 and 316.2 keV transitions are of equal $M1$ and $E2$ character, then the total K vacancy rate, excluding that associated with the 188.2 keV transition, is 1.555 ± 0.051. The difference between this value and the experimental K vacancy rate is the K vacancy rate associated with the 188.2 keV transition: 2.677(98) − 1.555(51) = 1.12(11). Thus, the K x-ray measurements reported in section 4.6 indicate that the 188.2 keV transition is approximately 100% $M1$ in character.

Another path to calculate the multipolarity of the 188.2 keV transition is through intensity balance. From figure 3, the terminus of the 188.2 keV transition is the excited state at 232.4 keV. The 168.3 and 137.7 keV transitions also terminate in this state, which deexcites

Table 20. Assigned photon multipolarities in the decay of $^{196}Au^{m2}$ and the calculated *K*-shell vacancy rate for each transition. The vacancy rate is calculated from the relative photon yield (table 7), the multipolarity of the transition and the resulting *K*-conversion coefficient [132, 133]. The multipolarity of the 263.8 keV transition is discussed in section 5.6. When more than one multipolarity contribute, the *K*-vacancy rates for both multipolarities are given.

Transition energy (keV)	Relative photon yield	Multipolarity	*K*-conversion coefficient	*K*-vacancy rate
84.7	0.01535 ± 0.00228	*E*3	0.477	0.0073 ± 0.0011
137.6	0.04525 ± 0.00102	*M*1	2.20	0.0996 ± 0.0022
147.8	1.2614 ± 0.0081	*E*2	0.353	0.4453 ± 0.0029
168.4	0.1736 ± 0.0014	*M*1	1.245	0.2161 ± 0.0017
174.9	0.01274 ± 0.00086	*M*4	59.7	0.761 ± 0.051
188.2	1.0	*M*1 and *E*2	0.912 and 0.198	0.912 and 0.198
263.8	0.03021 ± 0.00065	*M*1 and *E*2	0.358 and 0.084	0.0108 and 0.0025
285.5	0.11623 ± 0.00140	*E*2	0.0691	0.0080 ± 0.0001
316.2	0.08050 ± 0.00119	*M*1 and *E*2	0.219 and 0.0536	0.0176 and 0.0043

solely through the 147.8 keV transition. Using the sums of the coefficients for *K*-, *L*-, *M*-, and *N*-shell conversions [132, 133, 191] and the photon intensity data in table 20, the populating rate due to the 168.3 and 137 keV transitions is 0.60, while the depopulating rate due to the 147.8 keV transition is 2.59. This translates to a residual rate for the 188.2 keV transition of 1.99. The calculated *M*1 rate is 2.107, and the calculated *E*2 rate is 1.443, which results in a transition that is approximately 82% *M*1 in character.

The two methods used to calculate the multipolarity of the 188.2 keV transition are both impacted by the purity of the multipolarities assigned to the other transitions in the IT decay of $^{196}Au^{m2}$, particularly those of the 137.7 and 168.4 keV transitions. The effect of an admixture of *E*2 character in either or both of these transitions would cause the fractional probability of *M*1 character for the 188.2 keV transition to increase in both calculations. Wapstra *et al* [41] assigned shell-model configurations of $\pi 2d_{3/2}$ and $\nu 1i_{13/2}$ to both of the states involved in the 188.2 keV transition. A dominant *M*1 multipolarity would be expected for transitions between states with the same primary quantum numbers and a spin change of one.

5.6. Tentative placement of the 263.8 keV γ-ray in the ^{196}Au level scheme

The 263.8 keV γ-ray was assigned to the decay of $^{196}Au^{m2}$ based on its apparent half-life [41]. However, it was not observed to be coincident with other photons emitted in the decay, and it has not been placed in the level scheme.

The *Q*-value for the β^- decay of $^{196}Au^{m2}$ is 1.28 MeV [84]. It is sufficiently low that it is unlikely that a receiving state in ^{196}Hg exists to which decay would proceed with an observable rate, calculated from log *ft* values [192]. A 9.6 h component was not observed in the decay-curve analysis of the platinum *K* *x*-ray photopeaks (table 13) at a level of $\sim 10^{-4}$ of the magnitude of the 9.6 h component of the gold *K* *x*-rays, which is inconsistent with expectations for EC decay calculated from the intensity of the 263.8 keV photon. The level scheme of ^{196}Pt below the EC *Q*-value (2.10 MeV [84]) is well known [27], and no potential receiving states with appropriate J^π values have been observed. Also, emission of a 263.8 keV photon from a high-lying state populated in EC decay would be necessarily coincident with the emission of other γ-rays. Therefore, the 263.8 keV γ-ray must belong to

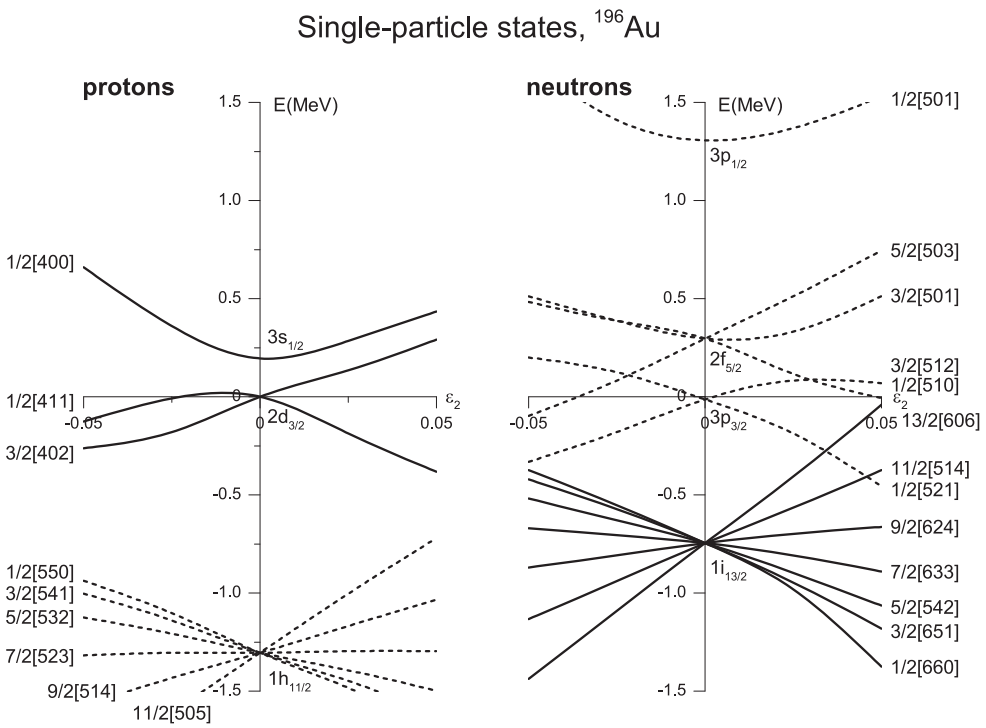

Figure 14. The odd-proton and odd-neutron single-particle states that couple to produce the energy levels in ^{196}Au below 1 MeV. The valence levels for both diagrams are placed at zero energy. The energy scale is derived from the harmonic-oscillator frequency, scaled to ^{196}Au.

the IT decay of ^{196}Au^{m2}, inserted into the ^{196}Au level scheme in the 596 keV interval between the metastable state and the ground state (see figure 3).

Relevant sections of the Nilsson diagrams for protons and neutrons as shown in figure 14 [81, 193–195] with energies scaled to ^{196}Au. The valence shell-model state at zero deformation is assigned zero energy in both diagrams. The metastable state arises from the parallel coupling of the $\pi 1h_{11/2}$ and $\nu 1i_{13/2}$ single particle states [60, 64]; other states arising from the coupling of these two states lie at higher excitation energies according to the Gallagher–Moszkowski rule [196] and do not provide a decay bridge to states of lower multipolarity. Examination of figure 14 indicates that the coupling of other single-particle proton and neutron states near the Fermi surface can produce angular momenta no greater than $J = 8$, making the only path for decay from the metastable state through a high-multipolarity transition as observed. If another $J = 8$ state existed in the ^{196}Au level scheme below the 420.8 keV state, most of the IT-decay intensity of ^{196}Au^{m2} would pass through it, which was not observed.

Since $\Delta J = 10$ between ^{196}Au^{m2} and ^{196}Au^{g}, it is highly unlikely that the 263.8 keV transition terminates in the $J^{\pi} = 2^{-}$ ground-state. It is more likely that the terminus is the 84.7 keV $J^{\pi} = 5^{+}$ ^{196}Au^{m1} state. Given the metastable character of ^{196}Au^{m1} ($t_{1/2} = 8.2$ s), a coincidence between the 84.7 and 263.8 keV photons emitted in cascade is not expected, consistent with observations [41]. The sum of the transition energies would require an excited state in ^{196}Au at (348.45 ± 0.07) keV, not proposed previously as being populated by the

radioactive decay of $^{196}Au^{m2}$. Experiments involving the scattering of charged particles [27, 42, 43] resulted in the identification of a state in ^{196}Au at (348.38 ± 0.06) keV with a multipolarity of $J^{\pi} = 5^{+}$ or 6^{+}; we propose that this state is the likely source of the 263.8 keV transition. The improved accuracy of the transition energy reported in table 4 was an important factor for confidence in placing the 263.8 keV γ-transition in the level scheme.

Three states in ^{196}Au at 420.6, 400.7, and 370.1 keV are connected through low-energy $M1$ and $E2$ transitions [41] that were unobserved in these experiments. The population of the level at 348.8 keV could originate from $M1$ and/or $E2$ transitions from some combination of these states, highly converted decays [132, 133, 191] of 72 keV, 52 keV, and 22 keV, respectively, that may have been too weak to provide an observable coincidence with the $M1$ ($E2$) 263.8 keV transition in the previous work [41].

6. Conclusions

The decay properties of radionuclides produced in the irradiation of ^{197}Au with fast neutrons have been measured, with an emphasis on the production of $^{196}Au^{m2}$. Measured values of the energies of the emitted photons agreed with the values reported in the literature, although the data associated with the EC decay of $^{196}Au^{g}$ have been improved. The half-life of $^{196}Au^{m2}$ was determined to be 9.603 h ± 0.23%. The relative intensities of the γ-rays were also measured, and a substantial change in the data associated with the IT decay of $^{196}Au^{m2}$ is warranted. The absolute intensity of the 188.2 keV γ-ray in $^{196}Au^{m2}$ decay is 0.3352 ± 2.9%; this transition was found to be predominantly $M1$ in character, as expected from previous measurements. The likely source of the 263.8 keV photon emitted in the decay of $^{196}Au^{m2}$ is a state at 348.4 keV, previously reported only in particle-scattering experiments.

A method for extracting the cross section for ^{197}Au$(n, 2n)^{196}Au^{g}$ at 14.1 MeV from the isotope inventory measured in a NIF irradiation was presented, based on a simulated neutron spectrum. The result was 1.98 b; in conjunction with the empirical $^{196}Au^{m2}/^{196}Au^{g}$ isomer ratio of 0.0731 ± 2.6%, a value of 2.124 b ± 2.6% for the ^{197}Au$(n, 2n)^{196}Au^{t}$ reaction was obtained, which agrees with the literature. The isomer ratio is sufficiently small that substantial changes in its value across the neutron energy window defined by the primary neutrons do not seriously impact the cross-section calculation. The cross section for the ^{197}Au$(n, p)^{197}Pt^{m}$ reaction at the same energy is approximately 1 mb.

The improved decay data for $^{196}Au^{m2}$ allow the comparison of diagnostic measurements of collected debris samples across a wide range of collection efficiencies with a reduced systematic bias. It improves the radiochemical diagnosis of NIF capsule performance, facilitates the development of other performance metrics (e.g. $^{196}Au^{m2}/^{196}Au^{g}$), and allows the exploration of potential effects of other physical processes in fusion plasmas with greater confidence.

Acknowledgments

The authors thank the NIF Diagnostics Group and NIF Engineering and Operations staff, as well as the staff of the LLNL Nuclear Counting Facility for help with the γ-ray spectrometry. This work was performed under the auspices of the US Department of Energy by Lawrence Livermore National Laboratory under Contract DE-AC52-07NA27344. This work was funded by the Laboratory Directed Research and Development Program at LLNL under project tracking code 16-SI-001.

ORCID iDs

N Gharibyan https://orcid.org/0000-0002-2604-2060

References

[1] Shaughnessy D A *et al* 2014 Radiochemical determination of inertial confinement fusion capsule compression at the National Ignition Facility *Rev. Sci. Instrum.* **85** 063508
[2] Moses E I, Boyd R N, Remington B A, Keane C J and Al-Ayat R 2009 The National Ignition Facility: ushering in a new age for high energy density science *Phys. Plasmas* **16** 041006
[3] Kucheyev S O and Hamza A V 2010 Condensed hydrogen for thermonucl. fusion *J. Appl. Phys.* **108** 091101
[4] Wilkens H L, Nikroo A, Wall D R and Wall J R 2007 Developing depleted uranium and gold cocktail hohlraums for the National Ignition Facility *Phys. Plasmas* **14** 056310
[5] Lindl J 1995 Development of the indirect-drive approach to inertial confinement fusion and the target physics basis for ignition and gain *Phys. Plasmas* **2** 3933–4024
[6] Boyd R N, Bernstein L and Brune C 2009 Studying nuclear astrophysics at NIF *Phys. Today* **62** 60
[7] Herrmann H W *et al* 2010 Diagnosing inertial confinement fusion gamma ray physics (invited) *Rev. Sci. Instrum.* **81** 10D333
[8] Lindl J D, Amendt P, Berger R L, Glendinning S G, Glenzer S H, Haan S W, Kauffman R L, Landen O L and Suter L J 2004 The physics basis for ignition using indirect-drive targets on the National Ignition Facility *Phys. Plasmas* **11** 339–491
[9] Hagmann C *et al* 2015 Note: radiochemical measurement of fuel and ablator areal densities in cryogenic implosions at the National Ignition Facility *Rev. Sci. Instrum.* **86** 076105
[10] Cerjan C, Springer P T and Sepke S M 2013 Integrated diagnostic analysis of inertial confinement fusion capsule performance *Phys. Plasmas* **20** 056319
[11] Frenje J A *et al* 2013 Diagnosing implosion performance at the National Ignition Facility (NIF) by means of neutron spectrometry *Nucl. Fusion* **53** 043014
[12] Pape S Le *et al* 2014 Observation of a reflected shock in an indirectly driven spherical implosion at the National Ignition Facility *Phys. Rev. Lett.* **112** 225002
[13] Glebov V Y *et al* 2006 Development of nuclear diagnostics for the National Ignition Facility (invited) *Rev. Sci. Instrum.* **77** 10E715
[14] Frenje J A *et al* 2010 Probing high areal-density cryogenic deuterium-tritium implosions using downscattered neutron spectra measured by the magnetic recoil spectrometer *Phys. Plasmas* **17** 056311
[15] Bleuel D L *et al* 2012 Neutron activation diagnostics at the National Ignition Facility (invited) *Rev. Sci. Instrum.* **83** 10D313
[16] McLane V, Dunford C L and Rose P F 1988 *Neutron Cross Section: Volume 2, Neutron Cross section Curves* (Cambridge, MA: Academic Press, Inc.)
[17] Prussin S G, Lane S M, Richardson M C and Noyes S G 1986 Debris collection from implosion of microballoons *Rev. Sci. Instrum.* **57** 1734–6
[18] Nakaishi H, Miyanaga N, Yamanaka M, Yamanaka T, Takagi M, Nakai S, Kobayashi K and Kimura I 1990 Experimental studies on debris collection for radiochemistry in inertial confinement fusion *Rev. Sci. Instrum.* **61** 2623–7
[19] Grim G P *et al* 2010 Target debris collection studies for inertial confinement fusion (ICF) experiments *J. Phys.: Conf. Ser.* **244** 032046
[20] Grim G P *et al* 2008 Prompt radiochemistry at the National Ignition Facility (invited) *Rev. Sci. Instrum.* **79** 10E503
[21] Eder D C, Koniges A E, Jones O S, Marinak M M, Tobin M T and MacGowan B J 2004 Late-time simulation of National Ignition Facility hohlraums *Nucl. Fusion* **44** 709
[22] Blue B E, Hansen J F, Tobin M T, Eder D C and Robey H F 2004 Debris mitigation in pinhole-apertured point-projection backlit imaging *Rev. Sci. Instrum.* **75** 4775–7
[23] Eder D C, Koniges A E, Landen O L, Masters N D, Fisher A C, Jones O S, Suratwala T I and Suter L J 2008 Debris and shrapnel mitigation procedure for nif experiments *J. Phys.: Conf. Ser.* **112** 032023

[24] Eder D C *et al* 2010 Assessment and mitigation of radiation, emp, debris & shrapnel impacts at megajoule-class laser facilities *J. Phys.: Conf. Ser.* **244** 032018
[25] Gostic J M, Shaughnessy D A, Moore K T, Hutcheon I D, Grant P M and Moody K J 2012 Solid debris collection for radiochemical diagnostics at the National Ignition Facility *Rev. Sci. Instrum.* **83** 10D904
[26] Emery J F and Leddicotte G W 1961 *The Radiochemistry of Gold* (Washington DC: U.S. Atomic Energy Commission) Number NAS-NS-3036
[27] Xiaolong H 2007 Nucl. data sheets for $a = 196$ *Nucl. Data Sheets* **108** 1093–286
[28] Taylor B N, Parker W H and Langenberg D N 1969 Determination of $\frac{e}{h}$, using macroscopic quantum phase coherence in superconductors: implications for quantum electrodynamics and the fundamental physical constants *Rev. Mod. Phys.* **41** 375–496
[29] Hankla A K, Fink R W and Hamilton J H 1972 Neutron activation cross sections at 14.4 MeV for some naturally occurring heavy elements in the region 76 z 82 *Nucl. Phys.* A **180** 157–76
[30] Zellermayer D M and Rosner B 1972 Isomeric cross-section ratios in the reactions ^{191}Ir(n, $2n$)^{190}Ir and ^{197}Au(n, $2n$)^{196}Au *Phys. Rev.* C **6** 315–20
[31] Ryves T B and Kolkowski P 1981 The Au(n,2n) and Au(n,γ) cross sections at 14 MeV *J. Phys.* G **7** 115
[32] Harston M R and Chemin J F 1999 Mechanisms of nuclear excitation in plasmas *Phys. Rev.* C **59** 2462–73
[33] Morel P, Daugas J M, Gosselin G, Méot V and Gogny D 2004 Nuclear excitation by electronic processes: NEEC and NEET effects *Proc. 6th Int. Conf. on Radioactive Nuclear Beams (RNB6): Nucl. Phys.* A **746** 608–12
[34] Kokta L 1973 Determination of peak area *Nucl. Instrum. Methods* **112** 245–51
[35] Falk W R 1984 Data reduction from experimental histograms *Nucl. Instrum. Methods* **220** 473–8
[36] Nuckolls J, Wood L, Thiessen A and Zimmerman G 1972 Laser compression of matter to super-high densities: thermonuclear (CTR) application *Nature* **239** 139–42
[37] Nuckolls J H 1982 The feasibility of inertial confinement fusion *Phys. Today* **35** 24
[38] Flerov G N, Gangrskii Y P, Markov B N, Pleve A A, Polikanov S M and Yungklaussen K 1968 *Sov. J. Nucl. Phys.* **6** 12
[39] Myers W D 1977 *Droplet Model of Atomic Nuclei* (New York: IFI/Plenum)
[40] Harper R C and Alford W L 1982 Experimental and theoretical neutron cross sections at 14 MeV *J. Phys. G: Nucl. Phys.* **8** 153
[41] Wapstra A H, Goudsmit P F A, Jansen J F W, Konijn J, Löbner K E G, Nijgh G J and de Wit S A 1967 The isomer with spin 12 in ^{196}Au *Nucl. Phys.* A **93** 527–44
[42] Wirth H-F *et al* 2004 One- and two-nucleon transfer reactions to ^{196}Au *Phys. Rev.* C **70** 014610
[43] Gröger J *et al* 2000 Nuclear structure of ^{196}Au: more evidence for its supersymmetric description *Phys. Rev.* C **62** 064304
[44] Van Isacker P, Jolie J, Heyde K and Frank A 1985 Extension of supersymmetry in nuclear structure *Phys. Rev. Lett.* **54** 653–6
[45] McMillan E, Kamen M and Ruben S 1937 Neutron-induced radioactivity of the noble metals *Phys. Rev.* **52** 375–7
[46] Bothe W and Gentner W 1937 Kernisomerie beim brom *Naturwissenschaften* **25** 284–284
[47] Snell A H 1937 The radioactive isotopes of bromine: isomeric forms of bromine 80 *Phys. Rev.* **52** 1007–22
[48] Wilkinson G 1948 Some isotopes of platinum and gold *Phys. Rev.* **73** 252–3
[49] Wilkinson G 1949 Radioactive isotopes of platinum and gold *Phys. Rev.* **75** 1019–29
[50] Van Lieshout R, Girgis R K, Ricci R A, Wapstra A H and Ythier C 1959 Characterization of the 10 h ^{196}Au isomer *Physica* **25** 703–7
[51] Ademollo M, Bocciolini M, di Caporiacco G and Mando M 1960 *Nuovo Cim.* **16** 1402
[52] Kavanagh T M 1960 Decay of Au^{196m} *Can. J. Phys.* **38** 1436–40
[53] Yule H P and Turkevich A 1960 Radiochemical studies of the (p, pn) reaction in complex nuclei in the 80–450 MeV range *Phys. Rev.* **118** 1591–8
[54] Ewbank W B, Marino L L, Nierenberg W A, Shugart H A and Silsbee H B 1960 Nuclear spins of six neutron-deficient gold isotopes *Phys. Rev.* **120** 1406–10
[55] Bergman O 1960 *Ark. Phys.* **18** 569
[56] Lingeman E W A, Löbner K E G, Nijgh G J and Wapstra A H 1962 The negaton transition in ^{196}Au *Nucl. Phys.* **31** 584–6

[57] Wapstra A H, Jansen J F W, Goudsmit P F A and Oberski J 1962 The decay of ^{196}Au *Nucl. Phys.* **31** 575–83
[58] Hobson J P, Hubbs J C, Nierenberg W A, Silsbee H B and Sunderland R J 1956 Spins of rubidium isotopes of masses 81, 82, 83, and 84 *Phys. Rev.* **104** 101–6
[59] Chan Y W, Ewbank W B, Nierenberg W A and Shugart H A 1962 Nuclear spin of 9.5 h au^{196m} *Phys. Rev.* **127** 572–3
[60] Bacon F, Kaindl G, Mahnke H-E and Shirley D A 1971 Magnetic moment of the 12-isomer of ^{196}Au *Phys. Lett.* B **37** 181–2
[61] Cunnane J C and Daly P J 1972 New high-spin isomer 2.3-day ^{198m}Au and the ^{198}Au level structure *Phys. Rev.* C **6** 1407–11
[62] Mahnke H-E, Kaindl G, Bacon F and Shirley D A 1975 Nuclear orientation of 2.3 d ^{198m}Au *Nucl. Phys.* A **247** 195–202
[63] Sakai K and Daly P J 1968 The decay of a new 18.7 h isomer of ^{200}Au *Nucl. Phys.* A **118** 361–8
[64] Bacon F, Kaindl G, Mahnke H-E and Shirley D A 1973 Nuclear magnetic resonance of oriented ^{196}Au, ^{198}Au, and ^{200m}Au *Phys. Rev.* C **7** 1654–63
[65] Hagn E and Zech E 1982 Nuclear magnetic moment of the 9.7 h 12-isomer ^{196m}Au *Nucl. Phys.* A **373** 256–66
[66] Chevarier N, Chevarier A, Demeyer A and Duc T M 1971 Réactions induites sur laor par des deutons de 10 à 70 MeV *J. Phys. France* **32** 483–90
[67] Casella V R 1975 Radiochemical studies of some low- and medium-energy nuclear reactions produced by accelerated tritions *Report* LA-5830-T Los Alamos National Laboratory
[68] Denisov V Y, Zheltonozhski V A and Reshitka S V 1993 *Yad. Fiz.* **56** 99
[69] Tárkányi F, Ditrói F, Hermanne A, Takács S, Király B, Yamazaki H, Baba M, Mohammadi A and Ignatyuk A V 2011 Activation cross-sections of deuteron induced nuclear reactions on gold up to 40 MeV *Nucl. Instrum. Methods* B **269** 1389–400
[70] Dzilavyan L Z, Lazareva L E, Ponomarev V N and Sorokin A A 1981 *Sov. J. Nucl. Phys.* **33** 308
[71] Rahman M S *et al* 2010 Measurement of isomeric-yield ratios for the ^{197}Au(γ,n)$^{196\ m,g}$Au reactions induced by bremsstrahlung *J. Radioanal. Nucl. Chem.* **283** 519–25
[72] Yokoyama A, Saito T, Shoji M, Baba H, Baba S, Hata K, Sekine T and Ichikawa S 1989 Nucleon transfer in highly mass-asymmetric reaction systems between 197Au and relatively light projectiles in the energy region below 10 MeV/u *Z. Phys.* A **332** 61–9
[73] Daub B H, Bleuel D L, Wiedeking M, Bernstein L A, Brickner N M, Brown J A, Goldblum B L, Holliday K S, Lundgren J and Moody K 2017 Neutron transfer in the ^{13}C +^{197} Au reaction from gold isotope residuals *Phys. Rev.* C **96** 024602
[74] Bonner N A, Goishi W, Hutchin W H, Iddings G M and Tewes H A 1962 Half-lives of tm^{167}, tm^{168}, tm^{170}, lu^{171}, lu^{172}, lu^{173}, lu^{174}, lu^{174m}, au^{195}, au^{196}, and au^{196m} *Phys. Rev.* **127** 217–9
[75] Karam R A, Parkinson T F and Ellis W H 1963 Final technical report on the nuclear properties of rhenium *Report* AD 402668 Department of Nuclear Engineering, University of Florida Appendix A
[76] Mangal S K and Khurana C S 1965 Isomeric (n, 2n) cross section ratios at 14.8 MeV *Nucl. Phys.* **69** 158–60
[77] Prestwood R J and Bayhurst B P 1961 (n, 2n) excitation functions of several nuclei from 12.0 to 19.8 MeV *Phys. Rev.* **121** 1438–41
[78] Tilbury R S and Yaffe L 1963 Nuclear isomers Hg^{197m,g}, Hg^{195m,g} and Au^{196m,g} formed by bombardment of gold with protons of energies from 8 to 60 MeV *Can. J. Chem.* **41** 2634–41
[79] Goldberg M D, Mughabghab S F, Purohit S N, Magurno B A and May V M 1966 Neutron cross sections volume iic, $z = 61$ to 87 *Report* BNL 325 Brookhaven National Laboratory 8
[80] Sethi B and Mukherjee S K 1968 Half-lives of the excited states of ^{46}Ti, ^{84}Rb, ^{99}Tc, ^{162}Dy, ^{164}Er, and ^{196}Au *Phys. Rev.* **166** 1227–33
[81] Firestone R B and Shirley V S (ed) 1996 *table of Isotopes* 8th edn (New York: Wiley)
[82] Rosner B, Felsteiner J, Lindeman H and Zellermayer D 1971 Lifetime and decay modes of the 84.6 kev isomer of ^{196}Au *Nucl. Phys.* A **172** 643–51
[83] Chattopadhyay R K, Bhattacharyya P, Sethi B and Tikku V K 1974 *Proceedings of the Nucl. Phys. and Solid State Physics Symposium* vol 17b (Bombay, India: Department of Atomic Energy) p 29
[84] Audi G, Wapstra A H and Thibault C 2003 The ame2003 atomic mass evaluation *Nucl. Phys.* A **729** 337–676 The 2003 NUBASE and Atomic Mass Evaluations

[85] Wang M, Audi G, Kondev F G, Huang W J, Naimi S and Xu X 2017 The AME2016 atomic mass evaluation (ii). tables, graphs and references *Chin. Phys.* C **41** 030003
[86] Plechatty E F, Cullen D E and Howerton R J 1975 Tables and graphs of photon interaction cross sections from 1.0 kev to 100 MeV derived from the lll evaluated nuclear data library *Report* UCRL-50400 Lawrence Livermore Laboratory vol 6
[87] Friedlander G, Kennedy J W, Macias E S and Miller J M 1981 *Nuclear and Radiochemistry* 3rd edn (New York: Wiley)
[88] Gharibyan N, Moody K J, Despotopulos J D, Grant P M and Shaughnessy D A 2015 First fission yield measurements at the National Ignition Facility: 14 MeV neutron fission of 238u *J. Radioanal. Nucl. Chem.* **303** 1335–8
[89] Murray G, Graham R L and Geiger J S 1965 The precision determination of some γ-ray energies using a β-spectrometer *Nucl. Phys.* **63** 353–82
[90] Knoll G F 2000 *Radiation Detection and Measurement* 3rd edn (New York: Wiley)
[91] Steinberg E P 1962 *Nuclear Instruments and Their Uses* ed A H Snell (New York: Wiley)
[92] Genoux-Lubain A and Ardisson G 1978 *Compt. Rend.* **287B** 69
[93] Helmer R G, Greenwood R C and Gehrke R J 1978 Reevaluation of precise -ray energies for calibration of Ge(Li) spectrometers *Nucl. Instrum. Methods* **155** 189–201
[94] Martin M J 2013 Nuclear data sheets for a = 152 *Nucl. Data Sheets* **114** 1497–847
[95] Reich C W and Cline J E 1970 Gamma-ray studies of the -vibrational band of ^{166}Er *Nucl. Phys.* A **159** 181–201
[96] Lingeman E W A, de Boer F W N and Meijer B J 1974 Intensities of -rays in the decay of ^{166m}Ho *Nucl. Instrum. Methods* **118** 609
[97] Larkins F P 1977 Semiempirical auger-electron energies for elements $10 = z = 100$ *At. Data Nucl. Data Tables* **20** 311–87
[98] Gunnink R and Niday J B 1971 Computerized Quantitative Analysis by Gamma-ray Spectrometry *Report* UCRL-51061 Lawrence Livermore Laboratory
[99] Gunnink R and Niday J B 1976 *ERDA Symposium of x- and gamma-ray Sources and Applications (Washington, DC)* (GPO) US Energy Research and Development Administration, CONF-760529
[100] Gunnink R, Ruhter W D and Niday J B 1988 GRPANL (GRouP ANaLysis): A suite of computer programs for analyzing complex Ge and alpha-particle detector spectra *Report* UCRL-53861 Lawrence Livermore Laboratory
[101] Davisson C M 1968 II - Interaction of radiation with matter *Alpha-, Beta- and Gamma-Ray Spectroscopy* ed K Siegbahn (Amsterdam: Elsevier) pp 37–78
[102] Moody K J 1983 *PhD Thesis* University of California, Berkeley, Lawrence Berkeley Laboratory Report LBL-16249
[103] Bevington P 1969 *Data Reduction and Error Analysis for the Physical Sciences* (New York: McGraw-Hill)
[104] Debertin K and Schötzig U 1977 Limitations of the pulser method for pile-up corrections in Ge(Li)-spectrometry *Nucl. Instrum. Methods* **140** 337–40
[105] Debertin K and Schötzig U 1979 Coincidence summing corrections in Ge(Li)-spectrometry at low source-to-detector distances *Nucl. Instrum. Methods* **158** 471–7
[106] Mignonsin E P 1994 Determination of half-lives by γ-ray spectrometry: Improvement of procedure and precision *Appl. Radiat. Isotopes* **45** 17–24
[107] Hubbell J H 1977 Photon mass attenuation and mass energy-absorption coefficients for H, C, N, O, Ar, and seven mixtures from 0.1 kev to 20 MeV *Radiat. Res.* **70** 58–81
[108] Reus U and Westmeier W 1983 Catalog of gamma rays from radioactive decay *At. Data Nucl. Data Tables* **29** 1–192
[109] de Vries C and Dijkstra J H 1960 Precision measurements of energies of gamma-rays following the decay of some gold isotopes *Nucl. Phys.* **18** 446–53
[110] Marklund I, Karlsson E and Korkman K 1962 *Ark. Fys.* **22** 289
[111] Jansen J F W and Pauw H 1967 Levels in ^{196}Pt from the decay of 6.2 d ^{196}Au *Nucl. Phys.* A **A94** 235–40
[112] Helmer R G, Greenwood R C and Gehrke R J 1971 Precise comparison and measurement of gamma-ray energies with a Ge(Li) detector. II: 400–1300 keV *Nucl. Instrum. Methods* **96** 173–96
[113] Kessler E G, Deslattes R D, Henins A and Sauder W C 1978 Redetermination of ^{198}Au and ^{192}Ir γ-ray standards between 0.1 and 1.0 MeV *Phys. Rev. Lett.* **40** 171–4
[114] Deslattes R D, Kessler E G, Sauder W C and Henins A 1980 *Ann. Phys. NY* **129** 378

[115] Helmer R G and van der Leun C 2000 Recommended standards for γ-ray energy calibration (1999) *Nucl. Instrum. Methods* A **450** 35–70
[116] Firestone R B 2007 Nucl. data sheets for $a = 24$ *Nucl. Data Sheets* **108** 2319–92
[117] Cabell M J and Wilkins M 1970 The half-lives of ^{198}Au and ^{148}Pm and the measurement of half-lives by γ-ray spectrometry *J. Inorg. Nucl. Chem.* **32** 1409–12
[118] Nichols A L 1990 X- and gamma-ray standards for detector efficiency calibration *Nucl. Instrum. Methods* A **286** 467–73
[119] Abzouzi A, Antony M S, Hachem A and Ndocko Ndongue V B 1990 Precision measurements of the half-lives of ^{60m}Co,^{79m}Se,^{104m}Rh,^{149}Nd,^{176m}Lu,^{177}Lu and ^{198}Au *J. Radioanal. Nucl. Chem.* **144** 359–65
[120] Unterweger M P and Lindstrom R M 2003 Ionization chamber measurements of the half-lives of ^{24}Na, ^{42}K, ^{76}As and ^{198}Au *Appl. Radiat. Isotopes* **60** 325–7
[121] Novkovic D, Nadderd L, Kandic A, Vukanac I, Durasevic M and Jordanov D 2006 Testing the exponential decay law of gold 198Au *Nucl. Instrum. Methods* A **566** 477–80
[122] Goodwin J R, Golovko V V, Iacob V E and Hardy J C 2007 The half-life of 198 Au: high-precision measurement shows no temperature dependence *Eur. Phys. J.* A **34** 271–4
[123] Campion P J and Merritt J S 1958 The half-life of na *Can. J. Phys.* **36** 983–6
[124] Genz H, Reisberg J, Richter A, Schmitz B M, Schrieder G, Werner K and Behrens H 1976 Determination of half-live, endpoint energy and shape factor in the decay of ^{27}Si and ^{24}Na with an on-line beta spectrometer *Nucl. Instrum. Methods* **134** 309–16
[125] Ikegami H, Sugiyama K, Yamazaki T and Sakai M 1963 Structure of platinum nuclei (i) new decay scheme of Au196 *Nucl. Phys.* **41** 130–58
[126] Elliott L G, Wolfson J L and Preston M A 1954 Disintegration of Au198 *Can. J. Phys.* **32** 153–66
[127] Volpe J and Hinman G 1956 Internal conversion in hg^{198} *Phys. Rev.* **104** 753–6
[128] Iwata Y and Yoshizawa Y 1980 Precision measurements of gamma-ray intensities iii: 52 Mn, 90Nb and 198Au *Nucl. Instrum. Methods* **175** 525–33
[129] Chand B, Goswamy J, Mehta D, Singh N and Trehan P N 1989 x-ray and gamma-ray intensity measurements in ^{131}I, ^{166}Ho, ^{198} Au and ^{199} Au decays *Nucl. Instrum. Methods* A **284** 393–8
[130] Xiaolong H and Chunmei Z 2005 Nuclear data sheets for a = 197 *Nucl. Data Sheets* **104** 283–426
[131] Bearden J A 1967 X-ray wavelengths *Rev. Mod. Phys.* **39** 78–124
[132] Hager R S and Seltzer E C 1968 Internal conversion tables part i: K-, l-, m-shell conversion coefficients for z = 30 to z = 103 *Nucl. Data* A **4** 1–11
[133] Kibédi T, Burrows T W, Trzhaskovskaya M B, Davidson P M and Nestor C W Jr. 2008 Evaluation of theoretical conversion coefficients using BrIcc *Nucl. Instrum. Methods* A **589** 202–29
[134] Broyles C D, Thomas D A and Haynes S K 1953 The measurement and interpretation of the k Auger intensities of sn^{113} , cs^{137}, and au^{198} *Phys. Rev.* **89** 715–24
[135] Larson H V, Myers I T and Roesch W C 1955 *Nucleonics* **13** 100
[136] Salem S I, Panossian S L and Krause R A 1974 Experimental k and l relative x-ray emission ratess *At. Data Nucl. Data Tables* **14** 91–109
[137] Krause M O 1979 Atomic radiative and radiationless yields for k and l shells *J. Phys. Chem. Ref. Data* **8** 307–27
[138] Cerjan C, Sayre D B, Landen O L, Church J A, Stoeffl W, Grafil E M, Herrmann H W, Hoffman N M and Kim Y 2015 Gamma reaction history ablator areal density constraints upon correlated diagnostic modeling of National Ignition Facility implosion experiments *Phys. Plasmas* **22** 032710
[139] Moran M J and Hall J 1997 Nuclear diagnostics in support of inertial confinement fusion experiments (invited) *Rev. Sci. Instrum.* **68** 521–6
[140] Rinderknecht H G *et al* 2012 A novel particle time of flight diagnostic for measurements of shock- and compression-bang times in D^{3}He and DT implosions at the NIF *Rev. Sci. Instrum.* **83** 10D902
[141] Clark D S *et al* 2015 Radiation hydrodynamics modeling of the highest compression inertial confinement fusion ignition experiment from the national ignition campaign *Phys. Plasmas* **22** 022703
[142] Hayes A C, Bradley P A, Grim G P, Gerard Jungman and Wilhelmy J B 2010 Reaction-in-flight neutrons as a signature for shell mixing in National Ignition Facility capsules *Phys. Plasmas* **17** 012705

[143] Bradley P A, Grim G P, Hayes A C, Jungman G, Rundberg R S, Wilhelmy J B, Hale G M and Korzekwa R C 2012 Neutron reactions in the hohlraum at the llnl National Ignition Facility *Phys. Rev.* C **86** 014617
[144] Chadwick M B and Derrien H 2019 ENDF/B-VIII.0 mat 1325 *Technical Report* 11 US Department of Energy
[145] Vonach H, Hille M, Stengl G, Breunlich W and Werner E 1970 Präzisionsmessung des al27 (n, α)-wirkungsquerschnitts für 14,43 MeV-neutronen *Z. Phys.* **237** 155–79
[146] Kudo K, Michikawa T, Kinoshita T, Kobayashi N, Fukuda A, Hino Y and Kawada Y 1987 Cross section measurements of ^{27}Al(n, α)^{24}Na and ^{56}Fe(n, p)^{56} mn reactions for neutron energies between 14.0 and 19.9 MeV *J. Nucl. Sci. Technol.* **24** 684–92
[147] Zhu C, Chen Y, Mou Y, Zheng P, He T, Wang X, An L and Guo H 2011 *Nucl. Sci. Eng.* **169** 188
[148] Sirakov I, Kopecky S and Young P G 2019 ENDF/B-VIII.0 mat 7925 *Technical Report* 11 US Department of Energy
[149] Vonach H K, Vonach W G, Munzer H and Schramel P 1968 Status of (n,2n) cross section measurements at bruyeres-le-chatel *Proc. Conf. on Neutron Cross sections and Technology* vol 2 *(Washington, DC)* (US National Bureau of Standards) p 885 NBS special publication 299
[150] Nethaway D R 1972 Cross sections for several (n, 2n) reactions at 14 MeV *Nucl. Phys.* A **190** 635–44
[151] Qaim S M 1972 Activation cross sections, isomeric cross-section ratios and systematics of (n, 2n) reactions at 14–15 MeV *Nucl. Phys.* A **185** 614–24
[152] Bayhurst B P, Gilmore J S, Prestwood R J, Wilhelmy J B, Jarmie N, Erkkila B H and Hardekopf R A 1975 Cross sections for (*n*, xn) reactions between 7.5 and 28 MeV *Phys. Rev.* C **12** 451–67
[153] Paulsen A, Liskien H and Widera R 1975 *Atomkernenergie/Kernt* **26** 34
[154] Veeser L R, Arthur E D and Young P G 1977 Cross sections for (*n*, 2*n*) and (*n*, 3*n*) reactions above 14 MeV *Phys. Rev.* C **16** 1792–802
[155] Frehaut J, Bertin A, Bois R and Jary J 1980 Status of (n,2n) cross section measurements at bruyeres-le-chatel *Proc. Symp. on Neutron Cross Sections from 10–50 MeV* (Brookhaven National Laboratory) pp 399–411
[156] Garlea I, Miron G, Dobrea D, Roth G, Musat T and Rosu H N 1984 *Rev. Roum. Phys.* **29** 421
[157] Greenwood L R, Guinan M W and Kneff D W 1985 Activation cross-section measurements at RTNS-II *Report* 0046-21 US DOE Fusion Energy
[158] Tewes H A, Caretto A A, Miller A E and Nethaway D R 1960 Excitation functions of neutron-induced reactions *Report* UCRL-6028T University of California
[159] Bayhurst B P and Prestwood R J 1961 (n,p) and (n,) excitation functions of several nuclei from 70 to 198 MeV *J. Inorg. Nucl. Chem.* **23** 173–85
[160] Dilg W, Vonach H, Winkler G and Hille P 1968 Messung von (n, 2n) wirkungsquerschnitten an schweren kernen *Nucl. Phys.* A **118** 9–16
[161] der Mateosian E and Goldhaber M 1957 Thermal-neutron activation cross sections of Ge and the isomeric ratio rule *Phys. Rev.* **108** 766–8
[162] Huizenga J R and Vandenbosch R 1960 Interpretation of isomeric cross-section ratios for (*n*, γ) and (γ, *n*) reactions *Phys. Rev.* **120** 1305–12
[163] Nagame Y, Sueki K, Baba S and Nakahara H 1990 Isomeric yield ratios in proton-, ^{3}-, and α-particle-induced reactions on ^{197}Au *Phys. Rev.* C **41** 889–97
[164] Barr D W, Browne C I and Gilmore J S 1961 Interpretation of experimental (*n*, 2*n*) excitation functions *Phys. Rev.* **123** 859–64
[165] NIELS Bohr 1937 Transmutations of atomic nuclei *Science* **86** 161–5
[166] Butler S T 1957 Direct nuclear reactions *Phys. Rev.* **106** 272–86
[167] Augustyniak W, Herman M and Marcinkowski A 1975 Cross sections for the (n, n′), (n, p) and (n, 2n) reactions on ^{107}Ag and ^{109}Ag isotopes *Nucl. Phys.* A **247** 231–7
[168] Thomas T D 1959 Cross section for compound-nucleus formation in heavy-ion-induced reactions *Phys. Rev.* **116** 703–12
[169] Blatt J M and Weisskopf V F 1952 *Theoretical Nuclear Physics* (New York: Wiley)
[170] Feshbach H, Porter C E and Weisskopf V F 1954 Model for nuclear reactions with neutrons *Phys. Rev.* **96** 448–64
[171] Moore R G Jr. 1960 Nuclear reaction cross-section theory *Rev. Mod. Phys.* **32** 101–16
[172] Biedenharn L C, Blatt J M and Rose M E 1952 Some properties of the racah and associated coefficients *Rev. Mod. Phys.* **24** 249–57
[173] Rose M E 1957 *Elementary Theory of Angular Momentum* (New York: Wiley)
[174] Liggett G and Sperber D 1971 Isomer ratio for (*b*, *xn*, *yp*, γ) reactions *Phys. Rev.* C **3** 447–54

[175] Vandenbosch R and Huizenga J R 1960 Isomeric cross-section ratios for reactions producing the isomeric pair $hg^{197,197m}$ *Phys. Rev.* **120** 1313–8
[176] Grover J R 1967 Shell-model calculations of the lowest-energy nuclear excited states of very high angular momentum *Phys. Rev.* **157** 832–47
[177] Cohen S, Plasil F and Swiatecki W J 1974 Equilibrium configurations of rotating charged or gravitating liquid masses with surface tension. II *Ann. Phys., NY* **82** 557–96
[178] Blann M 1980 Decay of deformed and superdeformed nuclei formed in heavy ion reactions *Phys. Rev.* C **21** 1770–82
[179] Lang D W 1966 The angular momentum-dependence of the nuclear level density *Nucl. Phys.* **77** 545–58
[180] Endt P M 1979 Strengths of gamma-ray transitions in $a = 6$–44 nuclei (iii) *At. Data Nucl. Data Tables* **23** 3–61
[181] Groening H, Aleklett K, Moody K J, McGaughey P L, Loveland W and Seaborg G T 1982 Isomer ratio measurements for the reaction ^{29}Si(^{18}O, p2n)$^{44\ m,\ 44g}$Sc *Nucl. Phys.* A **389** 80–92
[182] Groening H, Moody K J and Seaborg G T 1983 On the use of isomer ratios in ^{44}Sc for predicting spin populations in high energy heavy-ion nuclear reactions *Nucl. Instrum. Methods* **214** 317–20
[183] Andersson C G, Hellstrom G, Leander G, Ragnarsson I, Aberg S, Krumlinde J, Nilsson S G and Szymanski Z 1978 Islands of high-spin yrast isomers *Nucl. Phys.* A **309** 141–76
[184] Peck R A Jr 1957 *n*, *p*) reaction for gold *Phys. Rev.* **106** 965–71
[185] Coleman R F, Hawker B E, OaConnor L P and Perkin J L 1959 Cross sections for (n, p) and (n, α) reactions with 14.5 MeV neutrons *Proc. Phys. Soc.* **73** 215
[186] Haverfield A J, Easterday H T and Hollander J M 1965 Note on the Pt and Hg mass-197 isomers *Nucl. Phys.* **64** 379–92
[187] Drake D, Bergqvist I and McDaniels D K 1971 Dependence of 14 MeV radiative neutron capture on mass number *Phys. Lett.* **36B** 557–9
[188] Peto G, Csikai J, Long V, Mukherjee S, Banhalmi J and Miligy Z 1975 Radiative capture cross sections for 14.7 MeV neutrons *Acta Phys. Slovaca* **25** 185
[189] Magnusson G, Andersson P and Bergqvist I 1978 MeV neutron capture cross section measurements with activation technique* *Nukleonika* **23** 175
[190] Nemeth Z and Veres A 1990 Comparison of experimental and theoretical high multipole-order internal conversion coefficients *Nucl. Instrum. Methods* A **286** 601–6
[191] Dragoun O, Pauli H C and Schmutzler F 1969 Tables of internal conversion coefficients for n–subshell electrons *At. Data Nucl. Data Tables* **6** 235–351
[192] Gove N B and Martin M J 1971 Log-f tables for beta decay *At. Data Nucl. Data Tables* **10** 205–19
[193] Haxel O, Jensen J H D and Suess H E 1950 Modellmäßige deutung der ausgezeichneten nukleonenzahlen im kernbau *Z. Phys.* **128** 295–311
[194] Mayer M G 1950 Nuclear configurations in the spin–orbit coupling model: I. Empirical evidence *Phys. Rev.* **78** 16–21
[195] Gustafson C, Lamm I L, Nilsson B and Nilsson S G 1967 *Ark. Fys.* **36** 613
[196] Gallagher C J Jr and Moszkowski S A 1958 Coupling of angular momenta in odd–odd nuclei *Phys. Rev.* **111** 1282–90